metals

MDPI

Article

Laboratory-Scale Implementation of Standardized Reconstituted Geothermal Water for Electrochemical Investigations of Carbon Steel Corrosion

Stephanie Betelu [1,*], Chahinez Helali [1,2] and Ioannis Ignatiadis [1,*]

[1] French Geological Survey, BRGM, Water, Environment, Processes and analyses Division, 3 Avenue Claude Guillemin, 45060 Orleans, France; c.helali@brgm.fr
[2] LCA, INRAE, Toulouse INP, 4 allee Emile Monso, 31030 Toulouse, France
* Correspondence: s.betelu@brgm.fr (S.B.); i.ignatiadis@brgm.fr (I.I.); Tel.: +33-238-643-559 (I.I.)

Abstract: Currently, the demand for heat production by geothermal energy is increasingly strong amid the controversy surrounding non-renewable forms of energy. In France, the Dogger aquifer in the Paris Basin (DAPB) produces saline geothermal waters (GWs) that are hot (70–85 °C), anaerobic, and slightly acidic (pH 6.1–6.4), and are characterized mainly by the presence of Cl^-, SO_4^{2-}, CO_2/HCO_3^-, and H_2S/HS. These GWs are corrosive, while the well casings used are carbon steel. GWs have been continuously treated since the 1990s by corrosion inhibitors at the bottom of production wells to reduce water–steel interactions and scaling issues. Electrochemical experiments to optimize inhibitors were carried out on site, protected from the ambient atmosphere, with actual geothermal water, using water tapping at the wellhead. Currently, carbon steel corrosion/scaling, corrosion inhibition phenomenology, and kinetics evaluation remain important challenges. These issues are, of course, linked to the durability of installations. The novelty of our work consists of our validation of a modus operandi that properly reproduces, at the laboratory scale, operating conditions similar to those encountered on the types of geothermal installations. Particular attention was paid to characterizing waters and gases from 13 production wellheads that were modelled with PhreeqC® Version 3 hydrogeochemical software and the Thermoddem thermodynamic database for implementing standardized reconstituted geothermal water (SRGW), a well-balanced water representative of the major elements and dissolved gases of actual DAPB geothermal waters. The developed electrochemical setup enabled us to analyze corrosion mechanisms such as those observed on site and to investigate corrosion inhibition using petrosourced and biosourced inhibitors. The modus operandi constitutes a reference for further investigations, at the laboratory scale, of corrosion inhibition. These investigations may include screening and optimizing the formulas of petrosourced and biosourced inhibitors for use in DAPB waters.

Keywords: geothermal energy; carbon steel; corrosion; corrosion inhibition; electrochemistry; scanning electron microscopy; modeling

Citation: Betelu, S.; Helali, C.; Ignatiadis, I. Laboratory-Scale Implementation of Standardized Reconstituted Geothermal Water for Electrochemical Investigations of Carbon Steel Corrosion. *Metals* **2024**, *14*, 1216. https://doi.org/10.3390/met14111216

Academic Editor: Changdong Gu

Received: 26 August 2024
Revised: 10 October 2024
Accepted: 18 October 2024
Published: 25 October 2024

1. Introduction

Most of the geothermal installations in France exploit the low-enthalpy geothermal waters (GWs) of the Dogger Aquifer in the Paris Basin (DAPB).

The aquifer extends to depths of 1600–2200 m versus NGF, the general leveling of France and the precise measurement of the altitude of a point relative to the mean sea level. The temperatures of the anaerobic GWs range from 70 to 85 °C; their pH ranges from 6.1 to 6.4; and their redox potential ranges from −300 to −480 mV vs. the standard hydrogen electrode (SHE). The GWs of the DAPB are highly mineralized. The total dissolved solids (TDSs) vary from 6 to 35 g/L (ionic strength, 0.1−0.6 M). Much of these are Na^+ (3000−13,000 mg L^{-1}), Cl^- (5000−20,000 mg L^{-1}) [1], and SO_4^{2-} (300−1200 mg L^{-1}) [2]. The dissolved gases include mainly N_2, CO_2, H_2S, and CH_4. The concentrations of

CO_2/HCO_3^- range between 250 and 600 mg L^{-1}, and the concentrations of H_2S/HS^- range between 5 and 100 mg L^{-1} [2]. Systematic analytical studies have shown the existence of a sulfide-enriched zone (30–100 mg L^{-1}), mapped in 1994 and updated in 2011 [2], which extends from the north to the west of Paris; the rest of the GWs of the DAPB have much lower values (0–30 mg L^{-1}). In addition to the specific physical and chemical characteristics, sulfate- and thiosulfate-reducing bacteria are the main bacterial strains present in the GWs of the DAPB [3].

To heat buildings and to produce hot sanitary water, DAPB geothermal installations use two or three wells to pump and reinject saline waters. The warm waters flow from production well casings to the surface installations, where calories are extracted using heat exchangers. The cooled GWs are then reinjected several hundreds of meters further away, through one injection well or two injection wells, into the same DAPB. GW flows through the wells without releasing its gases, since the water production pressure, managed by an immersed pump at a depth of approximately −200 m, is always higher than that of the bubble point pressure. The exploitation flowrate ranges from 200 to 400 m^3/h, depending on the seasonal energy demand.

DAPB GWs have been exploited since the 1980s [4]. Since then, the vast majority of the 55 installations in the Paris Basin have used wells made of carbon steel (CS).

However, GWs' geochemical characteristics place them among the foremost corrosive natural waters for carbon steel [5]: CO_2/HCO_3^- and H_2S/HS^- acid–base pairs buffer DAPB waters at slightly acidic pH values; Cl^- and sulfide (S^{-II}) contents promote CS corrosion; and sulfate- and thiosulfate-reducing bacteria populations, by producing sulfide, accelerate it.

At the production temperature and pH of the GWs, dissolved inorganic carbon is able to produce very soluble corrosion products such as iron hydrogenocarbonate $Fe(HCO_3)_2$ and inhomogeneously distributed, less soluble, and more protective products such as iron carbonate $FeCO_3$ (siderite) [6–8]. At the same time, Cl^-, which is the most detrimental halide to Fe and its alloys, is adsorbed onto and transferred into corrosion by-products, leading to local accumulation, breaking down, and/or dissolving corrosion by-products. All these phenomena are responsible for localized corrosion [9–14] that is so intense that it appears generalized. Concomitantly, H_2S is able to stimulate both cathodic and anodic reactions in iron [15–17]. Moreover, high concentrations of S^{-II} are responsible for the formation of non-protective FeS deposits, depending on their crystallinity, for which the standard potential is higher than that of metal [6]. This phenomenon is responsible for increasing the number of active dissolution centers and activating the reduction process by promoting the discharge of H_2 [18,19]. In addition, sulfate- and thiosulfate-reducing bacteria that carry out anaerobic respiration using natural SO_4^{2-} and H_2 released from CS-XC38 corrosion [20] as their electron acceptor and donor, respectively, to produce H_2S/HS^- as a metabolic end product are able to accelerate the CS corrosion rate and biocorrosion process [21,22].

In the early 1980s, field experience demonstrated that, in production and injection wells, there was severe corrosion, deposit precipitation, and in some cases, partial clogging. This reduced the water production flowrate and caused a decline in energy production [4].

The inner layer of the polished sections of scales from different depths of geothermal wells in the Paris Basin was demonstrated by energy dispersive X-ray spectroscopy to be essentially formed of FeO(OH,Cl), $FeCl_2 \cdot 4H_2O$, $Fe_2(OH)_3Cl$, $FeCO_3$, and Fe_xS_y in small quantities [21]. The second, outside, layer was predominantly (80%) composed of iron sulfide, which was, for the most part, made up of mackinawite [23]. The other phases of iron sulfide, such as pyrite, marcasite, greigite, and pyrrhotite, were all present but in small proportions. An increase in the Cl^- content from the scale–solution interface towards the scale–metal interface confirmed the preponderant role of Cl^- in the activation of the corrosion process. It also suggested that Fe is most vulnerable during the development of the passive film; Cl^- incorporates into the film during the film thickening [24]. In agreement with publications in our bibliography [6,17,19], geographic zones with a high

sulfide content thus corresponded with those where there was extensive corrosion and clogging in the wells.

In order to improve the operating conditions of geothermal exploitation in the Paris region, the geothermal wells have progressively been treated, since 1989, using a well-bottom treatment tube (WBTT) with various pure or formulated petrosourced organic corrosion inhibitors (PS-OCIs) to prevent corrosion and scaling [21]. By selecting, inter-comparing, and optimizing pure or formulated PS-OCIs using on-site electrochemical techniques, it was found that corrosion inhibition efficiency ranged from 85 to 90% [25]. Because of the alterable physical and chemical characteristics of the fluid, experiments were necessarily carried out on site, protected from the ambient atmosphere, with actual geothermal water, using water tapping at the wellhead. The basic PS-OCIs were primary, secondary, and ternary amines; ethoxylated fatty amines; benzalkonium chloride; and quaternary ammonium salt-based formulations. Such formulations are still used for the continuous treatment of wells to reduce water–steel interactions and scaling issues. Currently, there are no further untreated fluids that can be used for testing the effectiveness of new OCIs, whereas carbon steel corrosion phenomenology and kinetics evaluation remain important challenges. In addition, there is a great need to test not only new PS-OCIs but also BS-OCIs (biosourced-OCIs) to improve geothermal exploitations, particularly since OCIs must be sufficiently effective at economically feasible concentrations, i.e., OCIs must be effective at very low concentrations (~2.5 mg L^{-1}) [21] and proven to present no risk of promoting localized corrosion. To make these exploitations more ethical, BS-OCIs should cause no issues to the ecosystem, since they are being introduced into GWs which are then returned to the environment.

Research must be continued in a laboratory setting, definitively in waters that are representative of those in the DAPB. The objective of this study is to set up geochemical and electrochemical modus operandi, at the laboratory scale, for investigating the mechanisms and kinetics of carbon steel corrosion and for optimizing carbon steel corrosion inhibition in a standardized reconstituted geothermal water (SRGW) of the Paris Basin. This SRGW must be a well-balanced water that is representative, in terms of the major elements and dissolved gases, of the DAPB's actual geothermal waters. The setup that we developed enabled us to assess and compare, according to common standards, the effectiveness of new molecules or formulations of PS-OCIs or BS-OCIs.

2. Materials and Methods

In-depth investigation and screening in the laboratory of carbon steel corrosion and inhibition in representative geothermal media require a systematic approach. For this purpose, functional carbon steel-based working electrodes have been designed, implemented, and adapted to monitor and investigate steel interfaces. Specific materials, as well as analytical equipment and techniques, have been selected and optimized to implement representative experiments, monitor the physical and chemical parameters of the fluid, and investigate corrosion and inhibition. Particular attention was paid to reconstituting a standardized DAPB geothermal water, named **SRGW** (standardized reconstituted geothermal water), that was a well-balanced water representative of the major elements and dissolved gases of actual DAPB geothermal waters.

2.1. Modus Operandi for the Reconstitution of a Representative Medium of the DAPB Waters

The SRGW was reconstituted thanks to the in-depth analytical characterization of the waters and gases from 13 production wellheads in the Val de Marne Department, located in the southeast of Paris, and via modeling using PhreeqC® Version 3 hydrogeochemical software and the ThermoddemV1.10_15Dec2020.dat thermodynamic database generated by BRGM [26]. PHREEQC Version 3 (United States Geological Survey, USGS.gov, https://www.usgs.gov/software/phreeqc-version-3, accessed on 5 December 2021) is a computer program, written in the C++ programming language, that is designed to perform a wide

variety of aqueous geochemical calculations. PHREEQC implements several types of aqueous models, including two ion-association aqueous models [27].

The geochemical model used for this purpose compiled the available data of the actual geothermal water in terms of the major and minor ionic elements, the non-conservative physicochemical parameters (temperature, pH, and redox potential), the non-conservative chemical composition (alkalinity, dissolved iron, dissolved sulfides, and mercaptans), the gas/liquid ratio (or GLR, in volume), and the content of free gases and dissolved gases. The bacterial and pressure factors were not included in the study regarding the time scale of each experiment (no more than 3 days). Biocorrosion is expected over longer periods than those investigated at the present in vitro laboratory scale. Moreover, previous studies on-site showed that the sulfate- and thiosulfate-reducing bacteria strains constitute an aggravating factor of the proper physico-electrochemical phenomena investigated here [21,22].

2.1.1. Analysis of Dissolved Species and Gases of Actual Geothermal DAPB Waters

The sampling and analytical methods used for the analyses of dissolved species and gases have been described in detail by Marty et al. (1988) [28] (for gases) and by Criaud et al. (1989) [29] (for dissolved species). Briefly, gas/liquid ratios were directly measured on site using volumetry. The gases were analyzed using gas-phase chromatography after the alkaline trapping of CO_2, whereas the aqueous species were analyzed using liquid-phase chromatography performed on acidified aliquots or using ICP/MS. The total dissolved sulfide content was determined in situ (detection limit 0.5 mg L^{-1}) with potentiometric titration, using a Tacussel TIM 900 Titralab (Radiometer Analytical, Villeurbanne, France) with a titrating solution of $Hg(NO_3)_2$ (5×10^{-3} or 5×10^{-4} mol L^{-1}) and using a specific silver sulfide electrode (Ag–Ag_2S) coupled to a Ag–AgCl reference electrode [30]. Alkalinity was also measured on site using potentiometric titration, with a titrating solution of HCl (1×10^{-1} mol L^{-1}) and using a combined pH electrode.

2.1.2. Physical and Chemical Characteristics of Actual Geothermal DAPB Waters

The physical and chemical characteristics of the 12 GWs investigated over a period of 2 years (2013–2014) from the department of the Val de Marne are presented in Appendix A, Tables A1 and A2.

Table A1 shows the average values of the main physical parameters and chemical elements. Table A2 presents the average percentage values of the main water dissolved and free gases. Tables A1 and A2 also show the average values and standard deviation calculated for each investigated parameter.

Each geothermal well exploiting the DAPB produces its own fluid. However, the fact remains that the fluids resemble each other on a regional level and locally. We thus decided to reproduce, at the laboratory scale, a well-balanced water composition that was representative in terms of the major elements and dissolved gases of actual DAPB geothermal waters. In Tables A1 and A2, the bold values highlight the parameters taken into account for the modeling of a DAPB-derived water sample whose chemical composition is representative of the major elements.

2.1.3. Modeling

Table A3 shows the content of minerals (in mM) and HCl 0.1 M (in mL) used for modeling the partial reconstitution of the ionic charge of the **prospective SRGW**, i.e., a water sample that is only representative of the major elements of actual DAPB geothermal waters.

Table A4 presents the parameters (pH, pe, temperature, ionic elements, and gas contents) inputted for modeling SRGW using the PhreeqC® hydrogeochemical software and the ThermoddemV1.10_15Dec2020.dat thermodynamic database [26]. On the left, at the bottom, Table A4 also shows the main parameters of the modeling output, i.e., the final pH, pe, elements, and contents (in mmol L^{-1} and in mg L^{-1}) in equilibrium with the N_2 (79.2%), CO_2 (20%), and H_2S (0.8%) gas mixture. These data are in the same order of magnitude as those of Tables A1–A3. The Table A4 parameters were, thus, used to

reconstitute an SRGW that takes into account, as much as possible, local DAPB geothermal water–carbon steel interactions.

2.1.4. Reconstitution

Table 1 presents the nature and mass of the mineral salts, provided by Sigma-Aldrich (St. Louis, MO, USA), to be weighed for the production of one liter of prospective SRGW that becomes SRGW after it is balanced, by continuous bubbling, with the following gas mixture: CO_2 (20%), H_2S (0.8%), and N_2 (79.8%) at 70 °C. The gas mixture was ordered from Air Liquide, Alfagaz^{TM}, Paris, France.

Table 1. Mineral salts' nature and mass used for the synthesis of 1 L of DAPB in Val de Marne.

Mineral Salts' Names and Formulas	Mass (g) for 1 L of Deionized Water
Sodium bicarbonate, $NaHCO_3$	0.44523
Potassium chloride, KCl	0.18637
Magnesium chloride hexahydrate, $MgCl_2$ $6H_2O$	1.8298
Ammonium sulfate, $(NH_4)_2SO_4$	0.07326
Calcium sulfate, $CaSO_4$ $2H_2O$	1.41632
Calcium chloride, $CaCl_2$ (anhydrous)	1.8868
Sodium chloride, NaCl	14.1645

Once equilibrated, the investigated corrosive medium, named SRGW, is a well-balanced water with the necessary salts for mimicking both the dissolved major elements (ionic activity and salinity) and the dissolved gases in the actual geothermal DAPB waters from the department of the Val de Marne.

2.2. Carbon Steel Working Electrode

2.2.1. Carbon Steel Grade

The well casings are manufactured from a grade of carbon steel selected according to the ANSI/NACE MR0175/ISO 15156 standard (materials for use in H_2S-containing environments in oil and gas production) [31]. The casings of the geothermal wells exploiting the DAPB are essentially made of API K55-grade carbon steel [4]. The material used and studied is the XC38-type carbon steel, which is a steel of a grade close to that of API K55 (Table 2). It is known for its moderate carbon content, which provides a balance of strength, ductility, and hardness. Its susceptibility to corrosion in acidic environments makes it an ideal candidate for evaluating the efficacy of corrosion inhibitors [32–36]. It is, in addition, of good machinability and sold under different shapes. It was, finally, the most cost-effective option.

Table 2. Comparison of the chemical compositions of the carbon steels CS-XC38 and CS-API K55.

Elements	Chemical Composition of CS-XC38 (% Mass)	Chemical Composition of CS-API K55 (% Mass)
C	0.38	0.42
Mn	0.65	1.08
Si	0.10	0.34
P	0.017	-
S	0.0116	0.004
Ni	0.050	0.092
Cr	0.03	0.10
Cu	0.062	-
Al	0.022	-
Fe	~98.6753	~98.3840

2.2.2. CS-XC38 Working Electrodes

The homemade, 20 cm high, CS-XC38 working electrode is presented in Figure 1. It is made of six machined parts (Figure 1A). The working CS-XC38 electrode is a cylinder of 7 mm diameter and 9 mm height with a central threaded hole (Figure 1B). In use, cylindrical electrodes proved to be more suitable than conventional disc-shape electrodes because of the robustness of the electrical contact, which is anchored to the carbon steel. Disc-shape electrodes are most often a small compressed spring, and the elastic modulus degrades over time due to continuous wear and tear. In addition, because of the cylindrical shape of the electrode, the surface was considerably improved with respect to external electrochemical disturbances. The measured roughness of the working electrodes ranges between 40 and 180 nm. Surface profile measurements were made with a diamond stylus profilometer. The lateral exposed surface ranges from 1.9 to 2.0 cm^2. The sensitive element is anchored to a threaded rod made of CS-XC38 with an external electrical contact that allows the insertion of a banana plug. The body carrier is a threaded cylinder of 9 mm diameter made of Kynar® polyvinylidene difluoride (PVDF) from Arkema (Colombes, France). This is a thermoplastic fluoropolymer with high temperature resistance, low permeability, and high mechanical strength that is used in applications requiring resistance to acids and hydrocarbons.

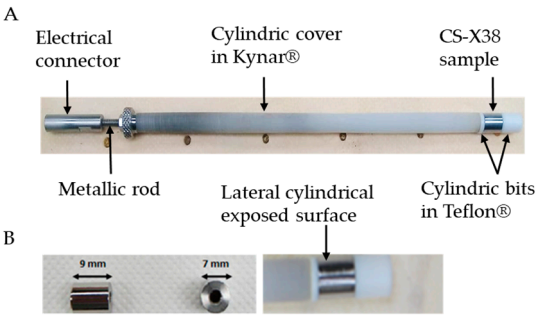

Figure 1. (**A**) Photograph of the CS-XC38 working electrode and its parts; (**B**) zoom on the dimensions and the lateral cylindrical exposed surface.

Two "disposable" PTFE (polytetrafluoroethylene, Teflon®) cylinders of 9 cm diameter, threaded in the center, sandwich the working CS-XC38 surface. This surface comprises a 3 mm thick puck and a 7 mm thick cap, three-quarters of which is threaded. The robust sealing between the working surface, the rod, and the body carrier is ensured by the two PTFE parts and an 8 mm thick threaded steel puck, which sandwiches the entire electrode body from top to bottom.

2.3. Experimental Setup

2.3.1. The Electrochemical Reactor

Experiments were conducted in a thermoregulated 1 L cylindrical Pyrex double-walled water-jacketed reactor at 70 °C ± 0.2 °C (Figure 2). A DC10–P5/U thermostat bath (ECO RE 415 S (LAUDA DR.R. WOBSER GMBH & CO. KG, Lauda-Königshofen, Germany) was used to control the temperature. The reactor was equipped with a cover that has seven conical holes. The following were inserted into these holes:

- A refrigerant, into which water flowing at 1 °C was used to condense vapors and minimize any losses of SRGW;
- Six essential electrodes which were used to monitor the physical and chemical parameters of the fluid and to investigate the reactivity of CS-XC38:
    - A commercial combined pH glass electrode (InLab Reach, Mettler Toledo, Colombus, OH, USA) that was systematically calibrated between each experiment using commercial standard buffer solutions (pH 4.006 (NIST/DIN), pH 7.00 (ANA) from Mettler Toledo® Colombus, OH, USA);
    - A platinum wire electrode, the open circuit potential (OCP) of which was monitored and compared to the internal reference of the pH electrode;

- An electrochemical triplet used only for electrochemical corrosion measurement and composed of the following: a CS-XC38 working electrode (WE); a saturated calomel reference electrode (SCE), which consists of a commercial SCE (K0077 from AMETEK, Inc., Berwyn, PA, USA) protected with a KCl 3 mol L^{-1} junction (K0065 from AMETEK, Inc., Berwyn, PA, USA); and a 6 cm high cylindrical Pt/Ir grid counter electrode (CE) with a diameter of 6 cm;
- One CS-XC38, referred to as the free electrode and used to monitor the reactor's OCP; this item was not exposed to external electrochemical disturbances;
- A Pyrex® tube glass bubbler comprising a dip tube and a diffuser. This was used for gas equilibration, i.e., of the humidified N_2 (79.2%), CO_2 (20%), and H_2S (0.8%) gas mixture, as otherwise stated.

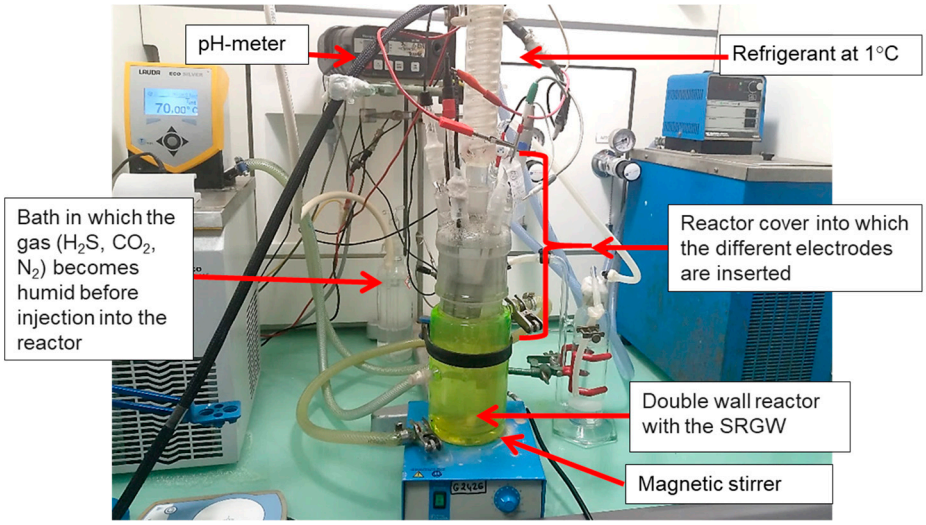

Figure 2. Experimental setup.

2.3.2. Electrochemical Apparatuses, pH Meter, and Data Logger

The electrochemical experiments used a PAR model 2273 potentiostat–galvanostat (AMETEK, Inc., Berwyn, PA, USA) interfaced to a PC system with PAR's PowerSuite v.2.58 software. A WTW pH meter (Xylem Analytical Europe, Weilheim, Germany), delivering output signals in volts for temperature and pH, was used and connected to a 3700A Data Acquisition System (Keithley Instruments, Inc., Cleveland, OH, USA) that was handled by a computer via KickStart–2 software, version 1.9.8 [37].

2.4. Electrochemical Techniques

From the beginning of its immersion in the SRGW, the electrochemical behavior of CS-XC38 was monitored using various electrochemical techniques.

Linear polarization resistance (LPR) and Tafel plots (TP) were measured by linearly polarizing the CS-XC38 electrode at ± 20 mV and at ± 200 mV, respectively, around OCP at a scan rate of 0.1 mV s^{-1} and 0.166 mV s^{-1}. Impedance measurements by electrochemical impedance spectrometry (EIS) were performed at the OCP of CS-XC38, over a frequency range of 1 MHz to 1 mHz, using perturbation signals with an amplitude of 10 mV [37].

The polarization resistance, R_p, was determined from the LPR curve ($R_{p(LRP)}$) [25] and the Nyquist plots of EIS measurements ($R_{p(EIS)}$) [37–39]. From the Nyquist plots, R_p was obtained by fitting the suitable equivalent circuit.

The corrosion current density (CCD), J_{corr} ($A.m^{-2}$), was calculated using the Stern–Geary equation Equation (1) [40,41]:

$$J_{corr} = \frac{B}{R_p \times A} = \frac{\beta_a \beta_c}{\ln(10) \times (\beta_a + \beta_c)} \times \frac{1}{R_p \times A} \quad (1)$$

where B is the Stern–Geary constant (V), R_p is the polarization resistance ($\Omega \cdot m^2$), A is the exposed (polarized) surface of steel (m^2), and βa and βc are the anodic and cathodic Tafel constants (V), respectively.

2.5. Gravimetric Analyses

The gravimetric technique was used to calculate the corrosion thickness loss of the surface area (S) of the carbon steel samples exposed to corrosive SRGW. It is based on the experimental determination of carbon steel weight loss (W_{loss}) by means of a chemical treatment, including an inhibitor in solution to minimize the overoxidation of the metal surface once the corrosion products have been fully eliminated. ASTM G1-90 (2017) was the standard norm applied for this work [42].

Detailed procedures can be found in our references [43,44]. CS-XC38 raw samples were first rinsed with milliQ 18 MΩ water and ethanol and then dried with compressed N_2 and weighed ($W_{before-exp}$, in g, is the weight of the sample before immersion). After CS-XC38's interaction with SRGW, the cylinders underwent desquamation. Corrosion products were removed by immersing the cylinders for 5 min in Clarke's solution (20 g antimony trioxide (Sb_2O_3), 50 g stannous chloride ($SnCl_2$), and 1 ml 38% hydrochloric acid (HCl)). Then, the cylinders were rinsed with milliQ 18 MΩ water and ethanol, dried with N_2, and weighed. The operation was repeated five times to determine the linear evolution of the mass versus time. The y-intercept is the representative mass of the sample after exposure to SRGW ($W_{after-exp}$, in g, is the weight of sample after exposure).

The corrosion thickness loss, CR_g (mm y^{-1}), is provided by Equation (2):

$$CR_g = \frac{W_{loss}}{\rho TS} \quad (2)$$

where W_{loss}, in g, is the weight loss ($W_{loss} = W_{before-exp} - W_{after-exp}$), ρ is the density of iron (0.00785 g·mm^3), S (in mm^2) is the exposed surface area, and T (in years) is the immersion time.

2.6. Electrochemical Study

Stationary (LPR and TP) and transitory (EIS) electrochemical techniques were consecutively applied to the CS-XC38 working surface, in a loop with a precise order and timing (Figure 3), to investigate the mechanisms of the interaction between CS-XC38 and SRGW in the absence and in the presence of inhibitors, in order to assess and to compare their inhibition effectiveness.

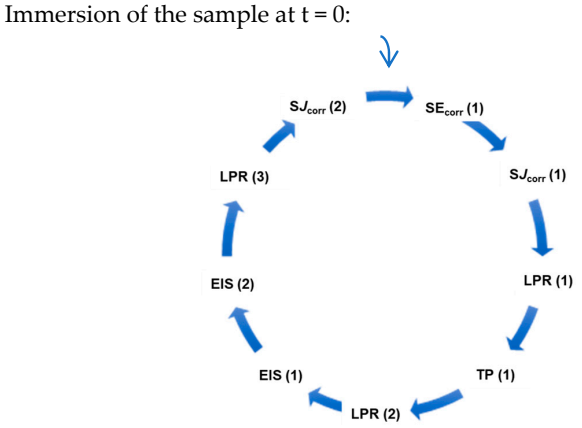

Figure 3. Schematic representation of an electrochemical analysis loop carried out on XC-38 steel samples; duration, ~3 h 55 min. SE_{corr}: monitoring of E_{XC38}, the open circuit potential of CS-XC38; SJ_{corr}: potentiostatic technique at E_{XC38} with monitoring of corrosion free-current density J_{corr} at the E_{XC38}; LRP: monitoring of R_p, allowing access to J_{corr}; TP: monitoring of E_{XC38}, J_{corr}, β_a, and β_c; EIS at E_{XC38}: monitoring of the CS-XC38 corrosion mechanism, monitoring of R_p, allowing access to J_{corr}.

EIS is based on the perturbation of an electrochemical system at steady state. In practice, the cell can change through adsorption/desorption phenomena, the growth/degradation of the coating layer, and the buildup of reaction products in solution. Two complementary impedances (EIS1 and EIS2) were frequently successively performed within a loop (ES1 from 1 MHz to 5 Hz and from 10 Hz to 1 mHz), and their data were merged to investigate both the repeatability and the stability of the measurement process throughout the time required to measure the EIS spectrum.

The loop was carried out about ten times (in the absence and in the presence of an inhibitor), c.f. Section 2.8. At the end of the fifth loop, the immersion duration reached approximately 19.63 h. An example of the adopted nomenclature for the treatment of the results is provided in Appendix B, Table A5, for five loops and includes the loop number and the name of the technique (with the technique, steel, sample number, content, date, and a number from 1 to 5 assigned by the equipment to designate the loop that was run). The measurement sequencing makes it possible to calculate the corrosion parameters as a function of the immersion time. It also allows the parameters to be averaged over the entire immersion period.

2.7. SEM Characterization

SEM was used to analyze the surface morphology of the CS-XC38 electrode, before any experiment and after 40 h of electrochemical disturbances into SRGW, in the absence and in the presence of inhibitors. For this purpose, immediately after the electrochemical experiments, the CS-XC38 electrodes were immersed in liquid N_2 to be transported to the microscope. The CS-XC38 working surfaces were unscrewed prior to insertion into the vacuum system. Surface morphology was studied using SEM, with secondary electron imaging using Tescan Mira 3 equipment coupled to energy dispersive X-ray (EDX) (Gaithersburg, MD, USA).

2.8. Petrosourced (PS) and Biosourced (BS) Organic Corrosion Inhibitors (OCIs); PS-OCI or BS-OCI

Ethylene glycol ($C_2H_6O_2$ anhydrous, 99.8%) was provided by Sigma-Aldrich. PEG-15 cocoamine was provided by PCC Group (Sienkiewicza, Poland). NORAM® was provided by Arkema (Colombes, France). The 8,14–Epoxy–17–Hydroxy–11,13(15)–Abietadien–16,12–olide (EHA) was provided by Terokit (Guangzhou, China). Pure 2–decenyl–2–oxazoline was synthetized by LCA, INRAE of Toulouse INP (Toulouse, France). The reaction, which was catalyzed by titanium tetrabutyl, consists of the amidation of undecylenic acid in the presence of ethanolamine, followed by cyclization.

PSIC is composed of 20% cocoamine 15 EO, 30% HEA, 30% $C_2H_6O_2$, and 20% H_2O.

PSIN is composed of 50% cocoamine 15 EO, 1.5% NORAM®, 0.5% $C_2H_6O_2$, and 43.5% H_2O.

BSID is pure 2–decenyl–2–oxazoline.

All the inhibitors were tested for an immersion time of 40 h, which is the best compromise between the time that can be devoted to an experiment (one inhibitor at one concentration) and the average persistence time of the best-performing PS-OCI used for the in situ treatment of the geothermal well of the DAPB. Experiments were performed at economically feasible concentrations.

3. Results and Discussion

3.1. Implementation of the SRGW

Figure 4A,B presents the temporal variation in T, pH, and the open-circuit potentials (OCPs) of Pt (E_{Pt}) and of CS-XC38 (E_{XC38}) during the implementation of the SRGW without an inhibitor and in the range of 0 to 10 h (Figure 4A) and 0 to 40 h (Figure 4B). OCPs are expressed in mV versus the standard hydrogen electrode (mV/SHE) at the investigated temperature. The reactor was filled with 1 L of deaerated (humidified N_2, 99.99999%, 1 bar) prospective SRGW continuously stirred at 25 °C. It was then equilibrated using a humidified N_2 (79.2%), CO_2 (20%), and H_2S (0.8%) gas mixture before the temperature

was raised to 70 °C to obtain the SRGW. Figure 4C shows the Eh–pH diagram during the preparation of the SRGW.

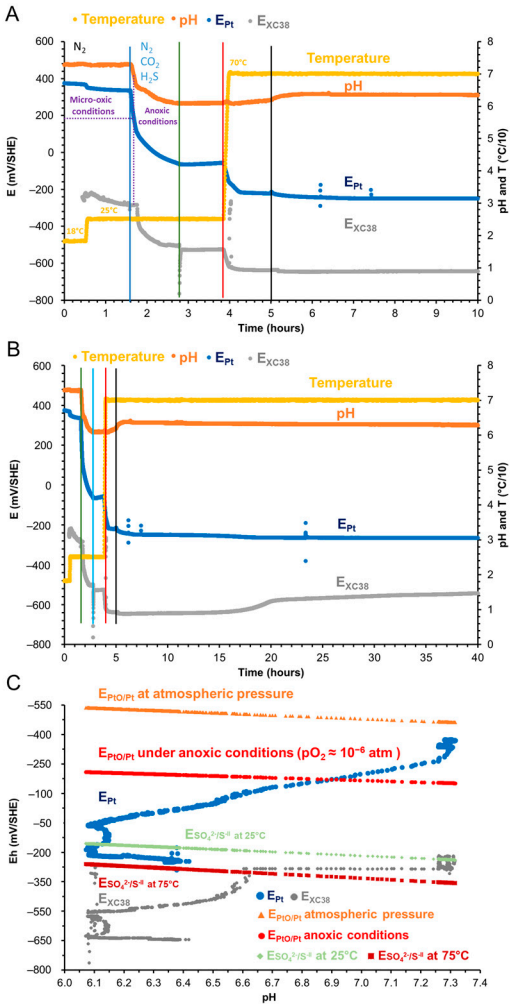

Figure 4. Temporal evolution of the physical and the chemical parameters (temperature, pH, E_{Pt}, and E_{XC38}) of the prospective SRGW (at 18 °C, 25 °C, and 70 °C) and SRGW (at 70 °C) during its preparation. (**A**) Temporal range: 0–10 h; (**B**) temporal range: 0–40 h; (**C**) Eh–pH diagram during the preparation of SRGW.

Figure 4A presents five distinct areas. The physical and chemical characteristics of the prospective SRGW equilibrated with humidified N_2 (100%) were observed between 0 and 1.6 h (blue vertical line). From 1.6 to 2.8 h (green vertical line), the SRGW was continuously bubbled with a N_2 (79.2%), CO_2 (20%), and H_2S (0.8%) gas mixture. After 2.8 h, bubbling was stopped (green vertical line) to investigate the present conditions of the prospective SRGW before increasing the temperature from 25 °C to 70 °C at 3.9 h (red vertical line). Beyond 5 h (black vertical line), the continuous bubbling was started again. Stopping bubbling in the range from 2.8 to 5 h made it possible to investigate the stability of both the prospective SRGW and the headspace. This also allowed for the minimization of the gas flow rate while maintaining the perfect SRGW saturation by the gas mixture.

During phase 1, E_{Pt} (351 ± 15 mV/SHE at pH 7.3, 25 °C) was fixed by the PtO/Pt redox couple under micro-oxic conditions (Figure 4C) [45]. At the same time, E_{XC38} reached –257 ± 20 mV/SHE. In agreement with the depletion of dissolved $CO_{2(g)}$ by N_2 (100%), the pH was fixed by the H^+/OH^- acid–base pair.

During phase 2, the addition of the two acid gases, H_2S and CO_2, was responsible for a pH decrease, in agreement with Equations (3) and (4):

$$H_2S + H_2O \leftrightharpoons HS^- + H_3O^+ \qquad pKa = 7.04 \tag{3}$$

$$CO_2 + 2H_2O \leftrightharpoons HCO_3{}^- + H_3O^+ \qquad pKa = 6.37 \tag{4}$$

Half of the equivalence of Equation (3) takes place at pH~7. In the pH range of 6.3–6.4, half of the equivalence of Equation (4) takes place. The pseudo-plateau observed for pH ranging from 6.2 to 6.1 is related to the theoretical completion of Equation (3), the equivalence of which occurred at pH 6.1 and 25 °C. For pH values inferior to 6.1, pH is fixed by the $CO_2/HCO_3{}^-$ acid–base pair.

Concomitantly, Pt electrode behavior is in quite good agreement with the acid–base reactions occurring in the prospective SRGW. In addition, the pseudo-plateau observed between −200 and −180 mV/SHE was attributed to the theoretical completion of Equation (5), the equivalence of which occurred at ~−180 mV/SHE at 25 °C (Figure 4C).

$$2O_2 + HS^- \text{ (or } + H_2S) \rightarrow SO_4{}^{2-} + H^+ \text{ (or } 2H^+) \tag{5}$$

In the pH range 7.3–6.9, E_{Pt} is a mixed potential fixed by the O_2/H_2O and $SO_4{}^{2-}/S^{-II}$ redox couples until reaching anoxic conditions, i.e., ~180 mV/SHE at pH 6.9 at 25 °C, $pO_2 \approx 10^{-6}$ atm [45] (Figure 4A,C). Beyond −180 mV/SHE, E_{Pt} is fixed by the $SO_4{}^{2-}/S^{-II}$ redox couple. From pH 6.1, it is fixed by $SO_4{}^{2-}/H_2S$.

Regarding CS-XC38, the addition of the two CO_2 and H_2S acid gases does not produce an instantaneous variation in OCP. Under the investigated conditions, this phenomenon is linked to the low activity of HS^-. The pH value reached ~6.6, for which $[HS^-] \approx [H_2S]$), when E_{XC38} exponentially decreased with pH until it reached −540 ± 57 mV/SHE at pH 6.1 at 25 °C. According to Iofa et al. 1964 [15], the increase in H_2S content accelerated the rate of CS-XC38's anodic dissolution, thereby shifting the corrosion potential to increasingly negative values. HS^- ions form a chemisorbed layer on the surface of the electrode; this layer acts as a surface catalyst, enhancing the kinetics of the iron dissolution reaction [15], Equation (6):

$$Fe + H_2S + H_2O \rightarrow (FeSH^-)_{ads} + H_3O^+ \tag{6}$$

According to Shoesmith et al. [46], the sorption reaction is followed by an oxidation step involving a two-electron transfer step, Equation (7). In this mechanism, depending on the experimental conditions, the produced $(FeSH^+)_{ads}$ could either convert to a corrosion product layer (Equation (8), i.e., an inhibition effect) or further hydrolyze to Fe^{2+} (Equation (9)) [33]:

$$(FeSH^-)_{ads} \leftrightharpoons (FeSH^+)_{ads} + 2e^- \tag{7}$$

$$(FeSH^+)_{ads} \leftrightharpoons FeS_{1-x} + xHS^- + (1–x)H^{+-} \tag{8}$$

$$(FeSH^+)_{ads} + H_3O+ \leftrightharpoons Fe^{2+} + H_2S + H_2O \tag{9}$$

During the exponential decrease, E_{XC38} was thus fixed by Fe^{II}/Fe, i.e., $(FeSH^+)_{ads}/Fe$, according to Equation (7), and/or Fe^{2+}/Fe, according to Equation (9). Then, a pseudo-steady state, reaching –540 ± 57 mV/SHE at pH 6.1 and 25 °C, was obtained, demonstrating that FeS_{1-x}/Fe redox couple fixes the OCP of CS-XC38 [47]; this observation was in agreement with the production of a layer of corrosion products (Equation (8)).

During phase 3, stopping the bubbling in the range from 2.8 to 5 h did not disturb either the physical and chemical parameters or the E_{XC38} (pH = 6.10 ± 0.01; EPt = −161 ± 5 mV/SHE; E_{XC38} = −540 ± 57 mV/SHE).

During phase 4, the increase in temperature was responsible for the increase in pH of 0.2 units because of the slight degassing of H_2S, while E_{XC38} immediately drastically decreased by ~100 mV and E_{Pt} remained stable for 12 min before decreasing by ~270 mV.

According to [48,49], the phenomenon observed in the CS-XC38, which is characterized by a sharp transition that is independent of the pH in the range of 1–7, is named the critical pitting temperature (CPT) and corresponds with the critical temperature at which

metastable pitting transforms into steady-state pitting. The governing mechanism for the observed temperature dependence of the pit potential was related to the formation of voids and the void-to-pore transition process; more specifically, related to this voiding process being influenced by the structural morphology of the coating and its dependence on temperature [9]. Below the transition point, void breakthrough is not sufficient to induce stable pitting and must act in concert with other components of an overall pit initiation mechanism. However, at temperatures above the transition point, void breakthrough might lead to the formation of pores that allow for a critical level of localized acidification and, thus, the initiation and propagation of stable pits [9]. During the generalization of the corrosion process, E_{XC38} can either be fixed by FeS_{1-x}/Fe, according to Equation (8), and/or by Fe^{2+}/Fe, according to Equation (9). E_{Pt} is fixed by SO_4^{2-}/H_2S at 70 °C; it is on the same order of magnitude and 50 mV higher (Figure 4C).

During phase 5, restarting the continuous bubbling of the gaseous mixture allows a balance to be reached rapidly. The pH value reached 6.31 ± 0.02 at 70 °C. At the same time, E_{Pt} evolves in agreement with the SO_4^{2-}/H_2S redox couple at 70 °C, until reaching −261 ± 6 mV/SHE (Figure 4B,C). In the pH range from 6.1 to 6.4, E_{XC38}= −39 × pH−396 mV/SHE, tending to demonstrate that the FeS_{1-x}/Fe redox couple fixes E_{XC38}. The increase in E_{XC38} from −640 to −573 mV between 15 and 20 h (Figure 4B) can be attributed to the covering of the steel with iron sulfide deposits that evolve in terms of crystallinity (in addition to FeO(OH,Cl), $FeCl_2.4H_2O$, and $Fe_2(OH)_3Cl$ corrosion products and, to a lesser extent, inhomogeneously distributed nano-$FeCO_3$). This finding is in agreement with in situ measurement [21] and geochemical modeling [47].

The continuous bubbling of the N_2 (79.2%), CO_2 (20%), and H_2S (0.8%) gaseous mixture in the prospective SRGW, at 70 °C, allows for the balancing of the physical and the chemical parameters (T = 70.3 ± 0.1, pH = 6.31 ± 0.02, E_{Pt} = –261 ± 6 mV/SHE). This occurs in agreement with the geochemical modeling for the obtainment of a stable SRGW versus time (Figure 4A,B and Table A4). These results validate the robustness of the setting up of the geochemical and electrochemical modus operandi for further investigating the mechanisms and kinetics of carbon steel corrosion and corrosion inhibition.

For subsequent experiments, the fully equipped reactor, except for the CS-XC38 electrodes, was filled with 1 L of prospective SRGW and continuously stirred at 25 °C. It was then equilibrated using the continuous bubbling of a humidified N_2 (79.2%), CO_2 (20%), and H_2S (0.8%) gas mixture before the temperature was raised to 70 °C. Once the physical and the chemical parameters reached the target values, the CS-XC38 electrodes were immersed in SRGW for electrochemical experiments in the absence and presence of PS-OCI or BS-OCI.

3.2. CCD in the Absence of Inhibitor

Figures 5–8 present the data of the electrochemical measurement carried out over 40 h by CS-XC38 immersed in SRGW: E_{XC38} versus SCE, LPR curves versus SCE, Tafel plots versus SCE, and EIS spectra at OCP, respectively. The polarization resistance (R_p) and corrosion current densities (CCDs) are presented in Table 3. The corrosion rates obtained by the gravimetric technique are discussed in Appendix C, Table A6.

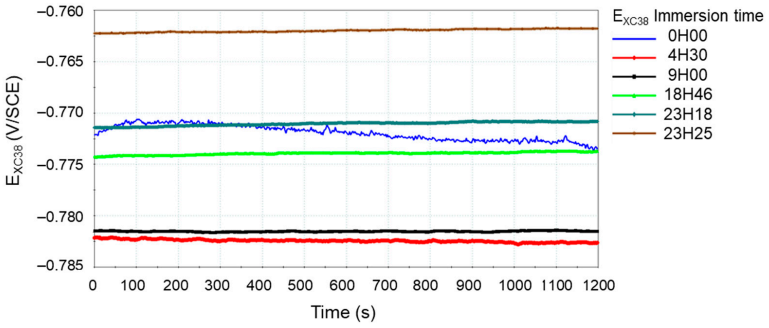

Figure 5. Evolution of E_{X38} as a function of time, when CS-XC38 was immersed in SRGW, in the absence of an inhibitor.

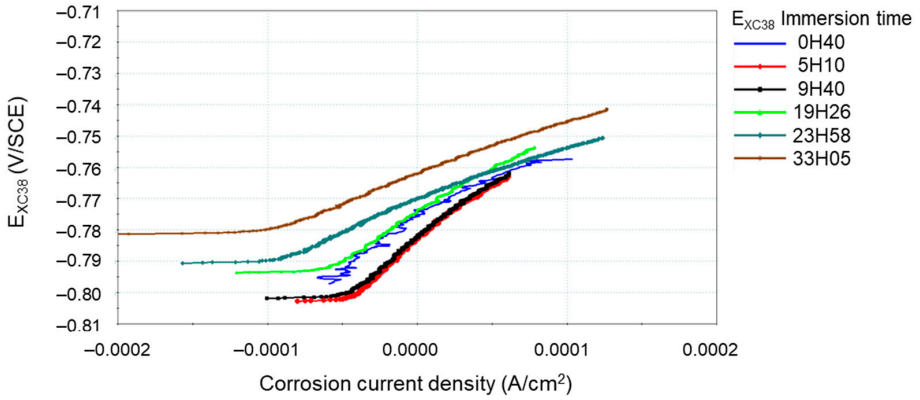

Figure 6. Evolution of the LPR curve of CS-XC38 as a function of time, when immersed in the SRGW, in the absence of an inhibitor.

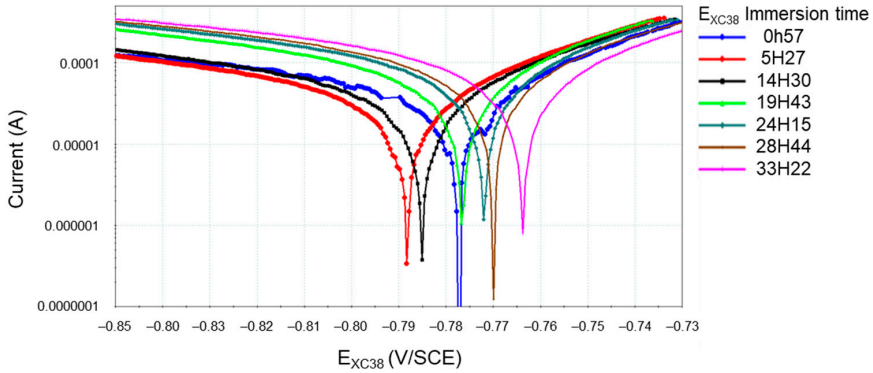

Figure 7. Evolution of the Tafel curves of CS-XC38 as a function of time, when immersed in the SRGW, in the absence of an inhibitor.

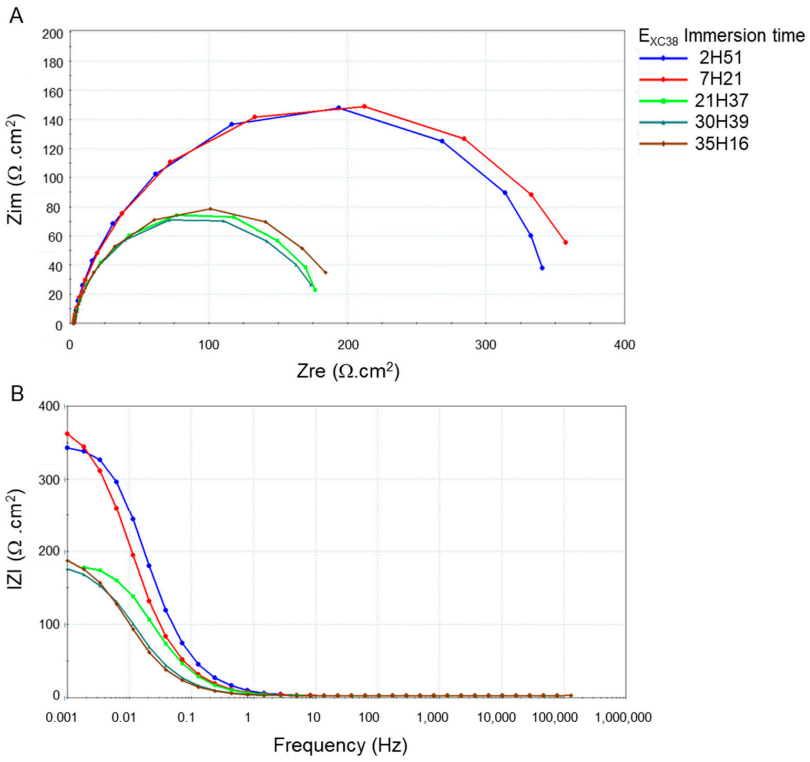

Figure 8. Evolution of EIS measurements during the immersion period of CS-XC38 in the SRGW, in the absence of an inhibitor. (**A**) Nyquist plot. (**B**) Bode plot.

Table 3. Temporal electrochemical parameters of CS-XC38 immersed in SRGW in the absence of an inhibitor.

E_{XC38} (mV/SCE)	Immersion Time (h)	$J_{corr\ (LRP)}$ ($\mu A\ cm^{-2}$)	$R_{p(LRP)}$ ($\Omega\ cm^2$)	$R_{p(EIS)}$ ($\Omega\ cm^2$)
−776	2	73	296	350
−784	6	57	383	371
−775	20	75	290	185
−772	25	117	186	193
−762	34	123	177	198

During the 40 h of immersion, four stages were distinguished.

The embrittlement of the steel begins immediately after the immersion (first stage). Indeed, from the first 300 s after immersion (Figure 5, blue line), the increase in $(FeSH^+)_{ads}$ content at the carbon steel interface is responsible for the decrease in E_{XC38} fixed by the $(FeSH^+)_{ads}$/Fe redox couple. The carbon steel corrosion process is governed by charge transfer (Figure 8, blue line, incomplete capacitive loop). R_p (Table 3) results from high anodic and cathodic activity (Figures 6 and 7, blue line). Indeed, Equation (7) is responsible for increasing the anodic activity by increasing the number of $(FeSH^+)_{ads}$ active sites. It is concomitantly responsible for the increase in cathodic activity, proving that interfacial H_3O^+ participates in the hydrogen reduction reaction, according to Equation (8).

The second stage endures over the first 10 h, where both E_{XC38} and R_p decrease (Table 3, Figures 6 and 8, red line). The sorption reaction is followed by an oxidation step resulting—according to the solubility product of iron sulfide, FeS (pKSFeS = 3.6)—in the covering of CS-XC38 by an amorphous, non-conductive thin film of iron sulfide (Equations (4) and (5)) that temporarily (~10 h) protects the steel. J_{corr} is decreased by 22% (Table 3 and Figure 7, red line versus blue line). The non-conductive thin film temporarily reduces the arrival of H_2S at the metal surface by blocking the active anodic sites (Figure 7, red line) and thus partially protects the steel surface against corrosion. The corrosion process is still increasingly controlled by the diffusion of H_2S through the thin deposit of iron sulfide (Figure 8, red line). This justifies the constancy of Tafel's cathodic coefficients (Figure 7, red line versus blue line). Meanwhile, because the deposit is relatively thin, it does not offer sufficient resistance to the diffusion of hydrogen sulfide and other substances responsible for attacking the steel (Cl^-, mainly). From that time onwards, the linear polarization curves (Figure 7) show a quasi-stability of anodic activity.

Within 10 h following immersion (third stage), E_{XC38} increases, whereas R_p decreases slightly (Table 3, Figures 5 and 6, black line). The limitation in the diffusion of H_2S through the deposit that caused the relative depletion of H_2S at the metal–deposit interface (Figures 7 and 8, red line) is responsible for the start of the crystallization of amorphous iron sulfide into mackinawite [21] (Figures 5–7, black line).

Beyond 10 h of immersion (fourth stage), E_{XC38} increased to −640 mV/ECS (Figure 5). The increase in iron sulfide deposits is responsible for the ennoblement of the CS-X38 steel (Figures 5 and 7). Measuring the electrochemical impedances of the electrodes shows that the polarization resistance decreases (Table 3) and the double-layer capacitance increases. The crystallization of amorphous iron sulfide into mackinawite is responsible for the corrosion rate increasing to high values (Table 3, Figures 6–8). Crystallization is accompanied by the activation of cathodic processes (Figure 7). The increase in the cathodic activity while the anodic activity remains quasi-stable results in a drop in the Tafel cathodic parameter. This is due to the transfer of cathodic sites from the surface of the steel to the surface of the conductive deposits; this transfer facilitates the discharge of hydrogen ions [18].

Due to HS^- sorption onto the anodic sites of the steel, SRGW produces the immediate embrittlement of the steel in the presence of dissolved H_2S (13–14 ppm). During the first hour of immersion, the instantaneous J_{corr} reaches 73 $\mu A\ cm^{-2}$ (assessed by R_p, Table 3). The sorption reaction is followed by an oxidation step, resulting in the formation of

an amorphous non-conductive iron sulfide thin film that temporarily (~10 h) diminishes the steel corrosion rate by >20%. The progressive increase and transformation of amorphous FeS into crystalline, conductive mackinawite results in a progressive, strong carbon steel attack that stabilizes at up to 123 µA cm^{-2} (assessed by R_p, Table 3).

Corrosion experiments on CS-XC38, in the absence of an inhibitor immersed in SRGW for 40 h, were repeated 10 times. Over the 40 h, the average values of 102 µA cm^{-2} (assessed by LRP), 66 µA cm^{-2} (assessed by TP), and 96.7 µA cm^{-2} (assessed by EIS) were calculated (Table 4) and used as references for the evaluation of the inhibition efficiencies of inhibitors when CS-X68 was immersed in SRGW for 40 h in the presence of PS-OCI and BS-OCI.

Table 4. Averages of Rps and CCDs calculated during the 40 h of immersion. Comparison between formulated PS-OCIs and pure BS-OCI.

Inhibitor	Content (mg L^{-1})	$R_{p(LRP)}$ (Ω)	$J_{corr(LRP)}$ (µA cm^{-2})	$IE_{(LRP)}$ (%)	$J_{corr\ (TP)}$ (µA cm^{-2})	$IE_{(TP)}$ (%)	$R_{p(EIS)}$ (Ω)	$J_{corr(EIS)}$ (µA cm^{-2})	$IE_{(EIS)}$ (%)
WI	0	234.9	102.2	/	65.7	/	243.5	96.7	/
PSIC	5	2002.3	10.6	**90**	1.3	**98**	2809.2	7.7	**92**
PSIN	5	2632.9	9.5	**91**	1.3	**98**	2560.4	8.9	**91**
BSID	5	2045.6	18.7	**81**	20.3	**79**	1757.1	21.1	**78**
BSID	20	1240.4	19.6	**80**	5.6	**94**	1987.0	11.0	**92**
BSID	160	5108.5	7.59	**92**	1.4	**98**	6284.6	4.2	**95**

3.3. SEM Characterization in the Absence of Inhibitor

Figure 9 compares SEM images for the raw CS-XC38 electrode and the CS-XC38 that was immersed in SRGW and electrochemically disturbed for 40 h. These images were obtained using secondary electrons (SEs), for the examination of the topography of the sample, and using backscattered electrons (BSEs), for the examination of the chemical contrast of the elements.

The raw CS-XC38 electrode surface is uniform (Figures 9A and 10, •1). After 40 h of immersion in SRGW, the surface deteriorated (Figure 9B). The scale thickness reached ~365 nm (Figure 9). EDX analysis performed on the scale showed that it is mainly composed of a mixture of FeS/FeS_{1-x} (Figure 10, •2); its morphology is shown in Figure 10. Despite the precautions carried out to minimize the oxidation of the corrosion products, the external surface of the scale shows the presence of oxidation products such as Fe^{II}/Fe^{III}–SO_4 double-layered hydroxides and $FeSO_4$ (Figure 10, •3). Their morphologies are shown in Figure 11.

3.4. CCD in the Presence of Inhibitors

The validation of the electrochemical modus operandi for investigating the mechanisms and kinetics of carbon steel corrosion in a laboratory enabled us to investigate corrosion inhibition using formulated petrosourced (PS) and pure biosourced (BS) organic corrosion inhibitors (OCIs), i.e., PS-OCIs or BS-OCIs (Table 4).

Table 4 presents the average polarization resistance (R_p) and CCDs calculated during the 40 h of immersion. Figures 12–14, for LPR curves versus SCE, Tafel plots versus SCE, and EIS spectra at OCP, respectively, illustrate the electrochemical behavior of each inhibitor when optimally adsorbed onto CS-XC38. The figures do not take into account the afterglow time (remanence time of the inhibitor), which differs from one inhibitor to another.

The slope of the potentiodynamic anodic and cathodic polarization curve for CS-XC38 shows that the addition of the petrosourced inhibitor PSIC at 5 mg L^{-1} shifted E_{XC38} to more positive values (Figures 12 and 13). These results indicate that PSIC acts as an anodic inhibitor. In the case of PSIN and BSID, the slight shift of E_{XC38} to positive values suggests that both behave as mixed-type inhibitors at the same concentration as PSIC.

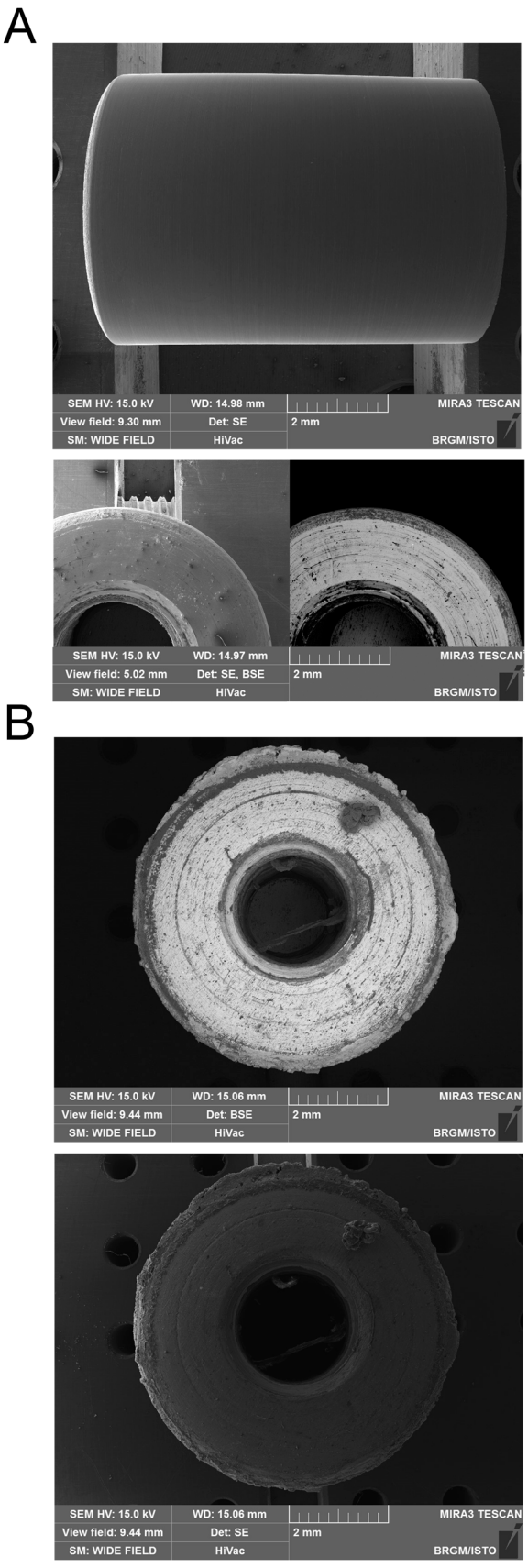

Figure 9. SEM images for (**A**) the raw CS-XC38 electrode and (**B**) the CS-XC38 electrode that was immersed and electrochemically disturbed for 40 h in SRGW.

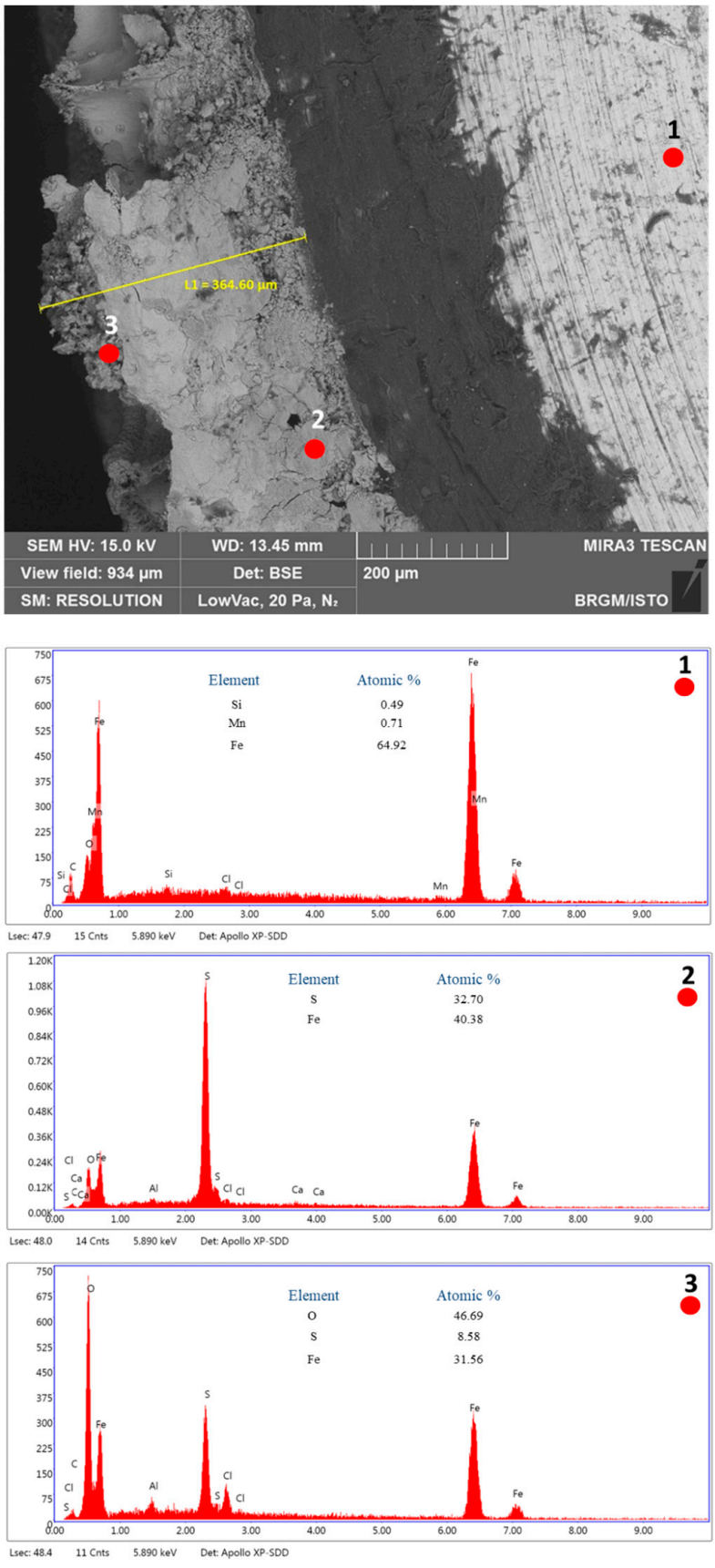

Figure 10. SEM–EDX analyses carried out on the CS-XC38 electrode that was immersed in SRGW and electrochemically disturbed for 40 h. Raw CS-XC38 surface (•**1**), internal scale (•**2**), external scale (•**3**).

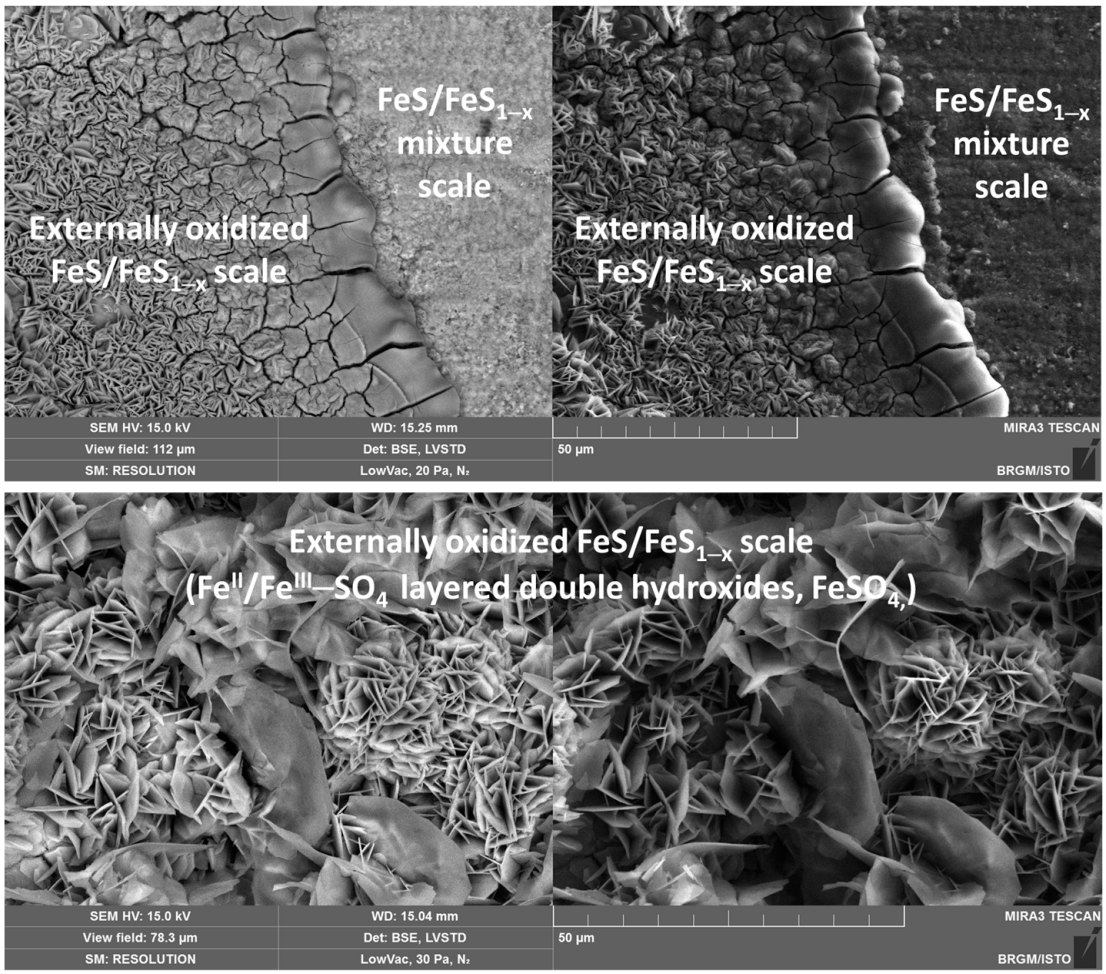

Figure 11. Zoom on the external surface of the scale coated on the CS-XC38 electrode after immersion in SRGW and 40 h of electrochemical disturbances.

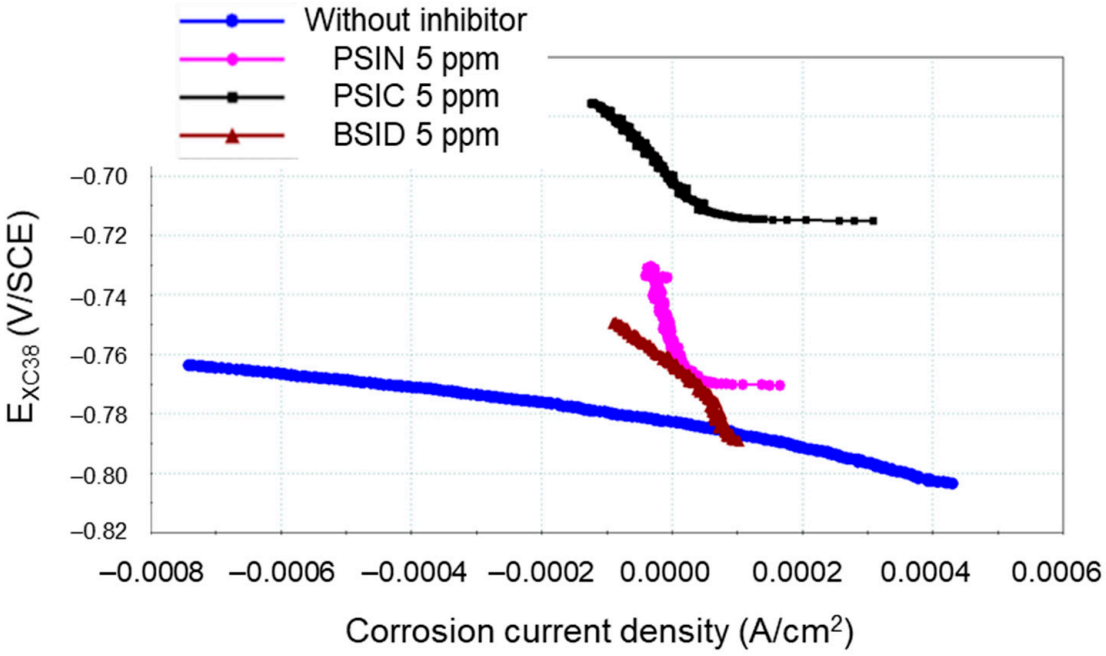

Figure 12. LPR when CS-XC38 is immersed in the SRGW in the absence and in the presence of formulated PS-OCIs and pure BS-OCI.

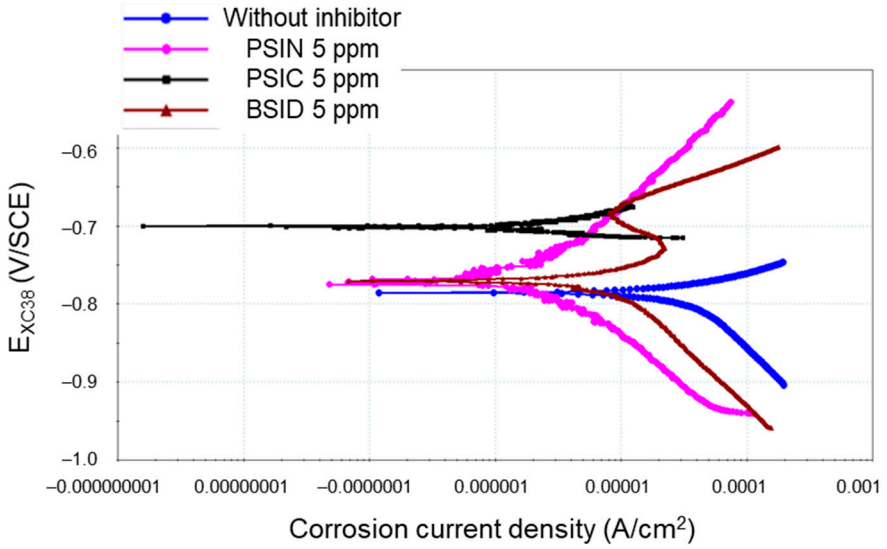

Figure 13. Tafel plots when CS-XC38 is immersed in the SRGW in the absence and in the presence of formulated PS-OCIs and pure BS-OCI.

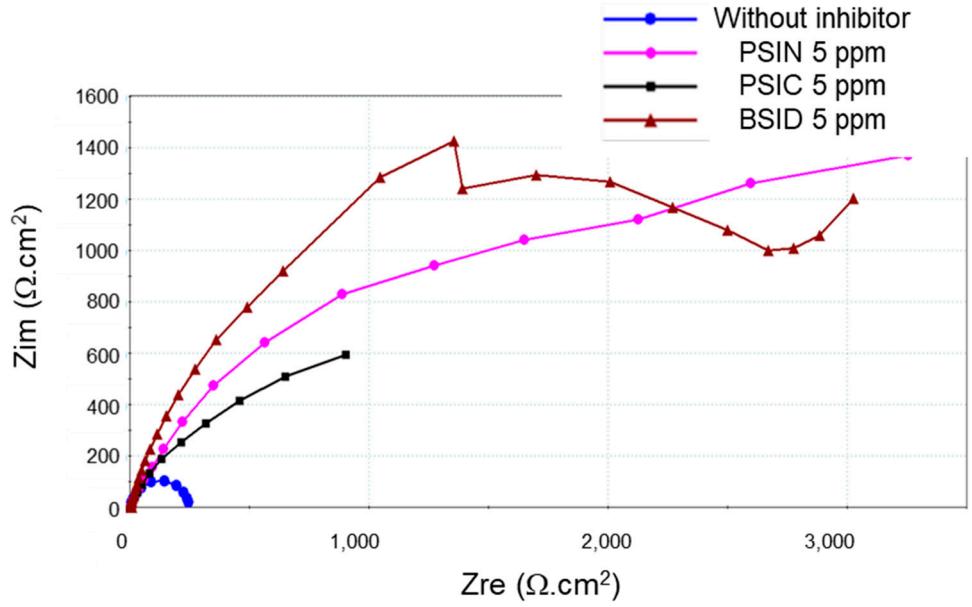

Figure 14. EIS Nyquist diagram when CS-XC38 is immersed in the SRGW in the absence and in the presence of formulated PS-OCIs and pure BS-OCI.

The EIS diagrams (Figure 14) show the changes in behavior in the carbon steel–SRGW interface in the presence of the inhibitor. The Nyquist diagram (Figure 14) shows that, in the absence of an inhibitor, the process is controlled by a charge transfer consisting of a perfect half-circle loop and a very low polarization resistance of around 243 ohms (Table 4). However, in the presence of inhibitors, a mixed process controlled the corrosion/inhibition. It involved a charge transfer and diffusion phenomena with higher R_p values (greater than 1757 ohm at 5 mg L^{-1}). The formation of a protective film on the metallic surface blocked the access to aggressive ions (mainly H^+ and Cl^-) by preventing amorphous iron crystallization.

The inhibition efficiency, IE (%), of both the petrosourced (PSIC and PSIN) and biosourced (BSID) inhibitors was calculated using Equation (10):

$$IE\% = \frac{J_{corr(WI)} - J_{corr(Inhibitor)}}{J_{corr(WI)}} \quad (10)$$

where $I_{corr(WI)}$ is the average CCD determined by each of the three methods used in the absence of the inhibitor, and $J_{corr(inhibitor)}$ is the average CCD, determined by each of the three methods, in the presence of a pure molecule or formulation.

The calculated values of IE (%) from the three CCDs ($J_{corr(LRP)}$; $J_{corr(TP)}$; $J_{corr(EIS)}$), as determined by each of the three techniques, are provided in Table 4.

3.5. SEM Characterization in the Presence of BSID

Figure 15A shows the distribution of the BSID inhibitor (20 mg·L^{-1}) on the CS-XC38 surface after immersion in SRGW and electrochemical disturbance for 40 h. It consists of thin, compact, and persistent stacked layers, thereby causing a quasi-uniform inhibitor distribution on the metal's surface. Its reaction to corrosion resistance was further supported by the SEM image (Figure 15B). The thickness of the scale reached ~12 µm, demonstrating that the presence of such an inhibitor reduces corrosion. Research is currently being carried out on the synthesis, investigation, and formulation of this family of BS-OCI compounds to ensure the sustainability of geothermal loops while minimizing health and environmental risks.

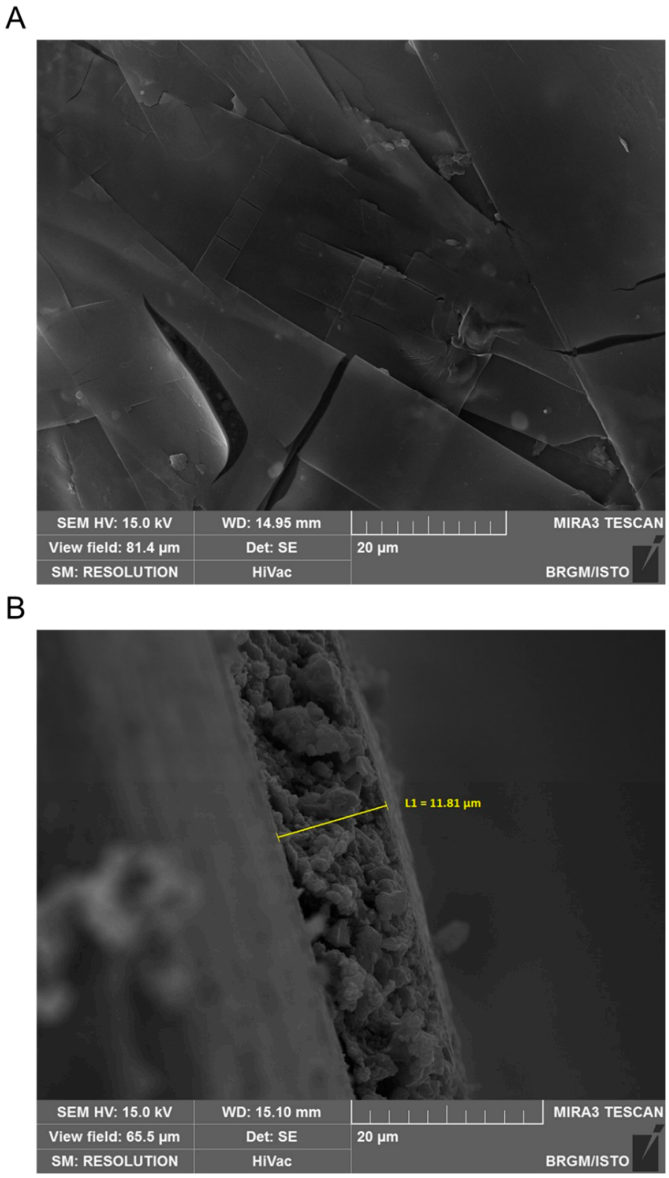

Figure 15. SEM images. (**A**) Morphology and distribution of the BSID inhibitor on the CS-XC38 surface after immersion in SRGW and electrochemical disturbances for 40 h. (**B**) Morphology and thickness (L1) of the corrosion scale.

4. Conclusions

The novelty of this work consists of its implementation and validation of a modus operandi that properly reproduces, at the laboratory scale, the operating conditions similar to those encountered on geothermal installations of the Dogger aquifer in the Paris Basin.

Particular attention was paid to producing a standardized reconstituted geothermal water (SRGW), a well-balanced water that was representative of the major elements and dissolved gases in actual geothermal waters of the DAPB. Specific materials, analytical equipment, and techniques were optimized to implement representative experiments, monitor the physical and chemical parameters of the fluid, and investigate corrosion and corrosion inhibition. Functional carbon steel-based working electrodes were updated to investigate the steel interface. The corrosion current density was determined from the electrochemical measurement of the polarization resistance, R_p, by linear polarization resistance (LPR), Tafel plots (TPs), and electrochemical impedance spectroscopy (EIS). TPs were selected to investigate the anodic and cathodic activities, and EIS was selected for an in-depth investigation of the interactions occurring at the carbon steel–SRGW interface.

The stable SRGW that was produced, in terms of the time that was required, its physical and chemical parameters (T, pH, and E_{Pt}), its chemical composition, and the chemical conditions of its gases, validated the robustness of our procedure.

The electrochemical setup that we developed enabled the analysis of corrosion mechanisms such as those observed on site. Additional SEM/EDX analysis confirmed this information. The SRGW was responsible for the immediate embrittlement of steel in the presence of dissolved H_2S (13–14 ppm) due to HS^- sorption into the anodic sites of the steel. The sorption reaction was followed by an oxidation step, resulting in the formation of a thin film of amorphous, non-conductive iron sulfide that temporarily (~10 h) diminished the steel corrosion rate (by about 25%). The progressive increase and transformation of amorphous FeS into crystalline, conductive mackinawite (pyrrhotite and pyrite in actual geothermal waters) resulted in a progressive and strong carbon steel attack.

The setup that we developed also enabled the assessment and comparison of the effectiveness of new molecules or formulations of PS-OCI or BS-OCI.

The modus operandi constitutes a reference for further investigations, at the laboratory scale, of corrosion inhibition. These investigations may include screening and optimizing the formulas of petrosourced and biosourced inhibitors for use in an SRGW that properly simulates DAPB waters.

Author Contributions: Conceptualization, S.B. and I.I.; methodology, S.B. and I.I.; software, all authors; validation, all authors; formal analysis, all authors; investigation, all authors; data curation, all authors; writing—original draft preparation, all authors; writing—review and editing, all authors; visualization, all authors; supervision, S.B. and I.I.; project administration, I.I.; funding acquisition, I.I. and S.B. I.I. is a co-director of the doctoral thesis of C.H.; S.B. is a co-supervisor of the doctoral thesis of C.H. All authors have read and agreed to the published version of the manuscript.

Funding: This work was supported by the French National Agency for Environmental and Energy Management (ADEME) as part of the INHIBIOSOURCE project (2017–2022), grant number 1782C0201. It was funded by BRGM, Orleans France (25%), and AQUAPROX Industries SAS, Levallois–Perret, France (75%), in the framework of a three-party scientific convention with the LCA and INRAE of Toulouse INP for the thesis administration (via the doctoral school EDSDM n°482) of Chahinez Helali (2020–2023).

Data Availability Statement: The original contributions presented in the study are included in the article, further inquiries can be directed to the corresponding authors.

Acknowledgments: The authors thank Cédric Duee (BRGM) for the SEM images; Romain Valentin, Zéphirin Mouloungui, and Sophie Thiebaud–Roux (LCA, INRAE of Toulouse INP) for the synthesis of 2–decenyl–2–oxazoline; and Jean–Yves Leguenic (SCODIP, Orleans) for fabricating the CS-XC38 electrodes.

Conflicts of Interest: The authors declare no conflicts of interest.

Appendix A

Table A1. Main average values of physical parameters and chemical ionic composition of actual geothermal waters at twelve production wellheads over a period of two years (2013–2014). Average values and standard deviations are presented for the parameters of the twelve geothermal waters. Values appearing in a 'blue' font colour were considered for geothermal water reconstitution.

Production Well	T	pH	E_h	Ω	P.Bulle	Salinity	Alcaline Reserve	Equiv HCO_3^-	S^{-II}	Fe^{2+}	Na	K	Ca	Mg	NH_4^+	HCO_3^-	Cl^-	SO_4^{2-}	B	SiO_2	F	Sr	Ba	Li
	(°C)		(mV/SHE)	(mS/cm)	(bar)	(eq. NaCl)	(mmol L^{-1})	(mg L^{-1})																
ADP(GADP-1)	72.4	6.44	−317	20.38	8.15	12.0	5.18	316.0	4.83	0.32	3916.12	63.59	472.53	107.77	15.54	322.61	6768.67	842.33	11.31	37.43	4.55	27.46	0.16	1.54
Alfortville (GAL-2)	69.9	6.34	−337	29.80	8.06	20.1	5.24	319.4	17.60	0.12	6335.53	92.98	942.20	211.25	21.77	299.85	11,453.95	858.49	12.34	41.77	4.20	52.12	0.29	2.44
Champigny GCHM-3	73.1	6.31	−300	41.83	9.2	28.0	4.75	290.0	9.91	1.43	8012.63	152.50	1229.28	239.70	26.70	280.00	15,633.75	905.00	17.34	38.48	2.70	67.05	0.35	3.14
Champigny GCHM-1	74.6	6.26	−329	36.06	8.39	26.6	5.36	327.1	12.52	0.27	8329.13	123.92	1297.32	264.08	25.22	290.14	15,357.67	886.25	13.48	41.70	3.96	67.13	0.35	2.77
Chevilly Larue GCHL-2	69.4	6.36	−339	23.03	7.48	16.7	5.09	310.3	14.00	0.06	5022.28	79.57	757.69	171.39	20.09	301.67	9414.16	796.55	11.05	40.34	4.52	42.63	0.24	1.94
Créteil GCRT-1	74.0	6.41	−300	35.79	7.79	21.8	4.86	296.3	18.18	1.15	6892.25	97.86	1074.44	222.08	23.31	291.26	12,433.91	841.08	12.06	42.16	4.83	54.64	0.28	
Fresnes GFR- 2	72.3	6.40	−336	20.84	7.77	13.0	5.23	319.0	13.27	0.16	4135.22	66.06	528.89	126.77	16.27	334.05	7157.26	901.26	9.58	38.53	4.12	28.74	0.18	1.61
L'Haÿ-les-Roses GHLR-2	70.5	6.38	−338	24.1	7.51	16.3	4.65	283.9	13.65	0.04	5150.74	79.55	731.32	169.65	19.48	307.47	9138.23	789.29	10.81	39.92	4.12		40.60	1.99
Orly 1 Gazier GORY-2	71.4	6.39	−323	23.77	6.4	15.9	5.20	317.5	8.06	0.28	5043.33	76.69	719.50	171.56	18.71	308.20	8833.70	806.47	10.96	41.32	5.68		40.42	
Orly 2 Nouvelet GORY-3	73.9	6.31	−342	23.77	8.52	14.9	5.90	360.0	9.58	0.11	4750.94	76.20	629.58	151.86	17.67	294.61	8290.49	814.77	10.14	38.96	4.18		32.64	1.77
Sucy en Brie GSUC-3	74.1	6.20	−325	39.32	9.81	25.9	4.62	282	14.97	0.96	8059.13	123.18	1278.63	245.01	26.77	284.81	1,5068.28	913.34	16.16	41.74	4.02		63.71	3.21
Thiais GTHI-1	73.8	6.35	−337	24.71	7.61	17.0	4.94	301.63	11.17	0.09	5361.22	82.92	785.29	175.67	19.17	293.64	9657.98	795.39	10.42	40.62	4.60		43.12	1.88
Average value	72.5	6.35	−326.9	28.62	8.06	19.0	5.1		12.31	0.42	5917.38	92.92	870.56	188.07	20.89	300.69	10,767.34	845.85	12.14	40.25	4.29		46.69	2.23
Standard deviation	1.8	0.1	14.6	7.6	0.88	5.4	0.4		3.86	0.48	1564.46	27.02	289.12	48.56	3.86	15.56	3178.22	46.36	2.40	1.58	0.69		14.17	0.62

Table A2. Average percentage values for the majority of the free gases (noted L (%) and dissolved gases (noted T (%) in actual geothermal waters at 12 production wellheads over a period of two years (2013–2014). Average values and standard deviations are presented for the percentage of gases in the 12 geothermal waters. Only the percentage values of CO_2 (16.256%) and H_2S (0.639%) and the sum of quasi-neutral gases N_2+Ar+He+CH_4+C_2+C_3+iC_4+nC_4+C_5+C_6 (85.772%) were considered for geothermal water reconstitution.

Geothermal Production Well	CO_2.L (%)	CO_2.T	AR.L (%)	AR.T	N_2.L (%)	N_2.T	HE.L (%)	HE.T	H_2S.L (%)	H_2S.T	CH_4.L (%)	CH_4.T	C_2.L (%)	C_2.T	C_3.L (%)	C_3.T	IC_4.L (%)	IC_4.T	NC4.L (%)	NC_4.T	C_5.L (%)	C_5.T	C_6.L (%)	C_6.T
ADP (GADP-1)	16.450		0.275		24.250		0.690		0.106		48.900		3.170		2.140		0.695		0.855		0.580		0.165	
Alfortville (GAL-2)	14.427	0.674	0.259	0.012	26.443	1.325	0.646	0.035	0.547	0.382	49.450	2.682	3.408	0.173	2.199	0.119	0.296	0.017	0.777	0.047	0.389	0.024	0.229	0.014
Champigny GCHM-3	17.300		0.230		29.500		0.710		0.058		42.800		3.310		2.010		0.240		0.590		0.350		0.120	
Champigny GCHM-1	16.216	0.859	0.438	0.029	29.491	1.619	0.744	0.042	0.608	0.378	45.465	2.510	3.471	0.190	2.014	0.111	0.268	0.015	0.628	0.035	0.355	0.019	0.198	0.012
Chevilly Larue GCHL-2	14.951	0.682	0.276	0.015	24.518	1.306	0.626	0.029	0.352	0.312	51.287	2.653	3.236	0.172	2.105	0.114	0.276	0.015	0.745	0.040	0.407	0.023	0.208	0.011
Créteil GCRT-1	15.666	0.896	0.240	0.013	25.695	1.412	0.509	0.028	0.225	0.200	49.065	2.688	3.503	0.191	2.147	0.117	0.298	0.016	0.772	0.042	0.449	0.025	0.239	0.013
Fresnes GFR-2	12.953	0.663	0.344	0.018	28.971	0.902	0.634	0.039	0.271	0.317	47.583	2.310	3.294	0.235	2.186	0.140	0.302	0.022	0.884	0.051	0.513	0.031	0.211	0.021
L'Haÿ-les-Roses GHLR-2	13.404	0.232	0.260	0.004	23.343	0.430	0.623	0.010	0.333	0.252	47.479	0.744	3.103	0.048	1.935	0.031	0.257	0.004	0.642	0.011	0.351	0.005	0.160	0.003
Orly 1 Gazier GORY-2	15.936	0.705	0.341	0.012	21.893	0.905	0.531	0.018	0.308	0.192	52.536	2.258	3.108	0.127	2.058	0.082	0.284	0.012	0.820	0.035	0.541	0.022	0.276	0.011
Orly 2 Nouvelet GORY-3	15.317	0.935	0.293	0.020	26.300	2.311	0.767	0.036	0.390	0.273	48.483	3.033	3.185	0.196	2.053	0.113	0.282	0.018	0.787	0.045	0.487	0.033	0.195	0.015
Sucy en Brie GSUC-3	19.360	1.173	0.226	0.014	27.480	0.108	0.720	0.006	0.578	0.341	43.780	0.018	3.266	0.080	1.980	0.047	0.240	0.006	0.630	0.015	0.368	0.009	0.128	0.000
Thiais GTHI-1	14.066	0.725	0.292	0.012	28.684	1.224	0.605	0.032	0.317	0.336	46.746	2.420	2.961	0.151	1.913	0.098	0.260	0.013	0.736	0.038	0.399	0.044	0.217	0.012
Average value	15.504	0.754	0.289	0.015	26.381	1.154	0.650	0.027	0.341	0.298	47.798	2.132	3.251	0.156	2.062	0.097	0.308	0.014	0.739	0.036	0.432	0.024	0.196	0.011
Standard deviation	1.76	0.24	0.06	0.01	2.53	0.62	0.08	0.01	0.17	0.07	2.84	0.96	0.16	0.06	0.09	0.03	0.12	0.01	0.10	0.01	0.08	0.01	0.05	0.01
Total gas	CO_2 (%)	16.26	AR (%)	0.30	N_2 (%)	27.53	HE (%)	0.68	H_2S (%)	0.64	CH_4 (%)	49.93	C_2H_6 (%)	3.41	C_3H_8 (%)	2.16	iC_4H_{10} (%)	0.32	nC_4H_{10} (%)	0.77	C_5H_{12} (%)	0.46	C_6H_{14} (%)	0.21
Gases considered for reconstitution	CO_2 (%)	16.26		H_2S (%)	0.64		AR (%) + NA(%) + HE (%) + CH_4 (%) + C_2H_6(%) +C_3H_8 (%) + iC_4H_{10} (%) + nC_4H_{10} (%) + C_5H_{12} (%) + C_6H_{14} (%)										85.77							

Table A3. Content of species (in mM) and HCl 0.1N (in mL) used for the partial reconstitution of the ionic charge of the prospective SRGW. Values appearing in a 'blue' font colour were considered for the reconstitution, while the difference between target and reconstituted species concentration values are given (in mM).

	Elements (mM)							
Mineral or Addition	**Ca**	**Mg**	**Na**	**K**	**NH_4^+**	**HCO_3^-**	**Cl**	**SO_4^{2-}**
$NaHCO_3$			5.300			5.300		
KCl				2.500			2.500	
$MgCl_2$		9.000					18.00	
$(NH_4)_2SO_4$					1.16			0.58
$CaSO_4$	8.226							8.226
$CaCl_2$	17.000						34.00	
NaCl			242.371				242.371	
HCl 0.1 N 1 mL							0.1	
Reconstituted value (mM)	25.226	9.000	247.671	2.500	1.160	5.300	296.971	8.805
Targed value (mM)	21.722	7.738	197.318	2.377	1.158	4.929	303.707	8.805
Reconstituted vs targed gap (mM)	3.5	1.3	50.4	0.1	0.0	0.4	-6.7	0.0

Table A4. Left: software, thermodynamic database, and initial parameters used for the hydrochemical modeling of the SRGW. Right: gas mixture composition used for modeling, and main parameters and ionic composition obtained after hydrochemical modeling.

Phreeqc Interactive 3.7.3–15968 **Thermodynamic Database Used:**
ThermoddemV1.10_15Dec2020.dat
Geothermal Solution 1
pH 6.3 charge
pe 4 temp 70
units mmol L^{-1}
Ca 25.226
Mg 9
Na 247.3
K 2.5
N(−3) 1.158
C(4) 4.929 as HCO3
Cl 296.871
S(6) 8.805
save geothermal solution 1
end
Use geothermal solution 1
EQUILIBRIUM_PHASES 1 CO_2(g) –0.698970004 # 20.0%
H_2S(g) –2.096910013 # 0.8%
N_2(g) –0.101274818 # 79.2%
end

Gas Mixture Composition Used for Modeling	
CO_2 (%)	20.0
H_2S (%)	0.8
N_2 (%)	79.2

Main Parameters and Content Obtained after Modeling		
pH	6.248	
pe *	−3.419	
Elements	**[content] (mM)**	**[content] (mg L^{-1})**
$C(4)_{tot}$	7.19	86.32
HCO_3^-	3.70	225.52
Ca	25.69	1029.60
Cl	302.40	10720.99
K	2.55	99.54
Mg	9.17	222.78
N	0.94	13.14
Na S_{tot}	251.90 9.18	5791.12 294.21
S^{-II}	0.58	18.55
H_2S	0.35	11.84
HS^-	0.23	7.64

* pe is a dimensionless number. It can easily be related to E_H by the following equation:

$$pe = E_H \times V_T \times \lambda$$

where $V_T = RT/F$ is the thermal voltage, R is the gas constant (8.314 $J \cdot K^{-1} \cdot mol^{-1}$), T is the absolute temperature in Kelvin, and F is the Faraday constant (96 485 coulomb mol^{-1} of e^-). Lambda, $\lambda = \ln(10) \approx 2.3026$.

Appendix B

Table A5. Typical example of electrochemical experiments on CS-XC38 immersed in SRGW and treated with 2.5 mg L^{-1} of Testname. The following nomenclature was adopted: loop number, name of the technique (technique, steel, sample number, inhibitor content in 2.5 mg L^{-1}, date, followed by a number from 1 to 5, both assigned by the apparatus to designate the current loop). The immersion time column provides, in hours, the time to start the technique. We can deduce, by the difference between times, the time spent on each technique and the duration of the pause before starting another technique.

Loop Number	Technique	Date, hour	Time per Technique	Ommesrion Time (h)
1	EXC38_3_2.5_TESTNAME_161120_1	16/01/2024 12:27:00	0:00:00	0.00
	PSXC38_3_2.5_TESTNAME_161120_1	16/01/2024 12:38:40	0:21:36	0.36
	RPXC38_3_2.5_TESTNAME_161120_1	16/01/2024 13:00:16	0:32:43	0.55
	TaXC38_3_2.5_TESTNAME_161120_1	16/01/2024 13:11:23	0:44:31	0.74
	RPXC382_3_2.5_TESTNAME_161120_1	16/01/2024 13:23:11	2:01:23	2.02
	Z1XC38_3_2.5_TESTNAME_161120_1	16/01/2024 14:40:03	2:13:08	2.22
	RPXC383_3_2.5_TESTNAME_161120_1	16/01/2024 14:51:48	3:34:38	3.58
	PSXC382_3_2.5_TESTNAME_161120_1	16/01/2024 16:13:18	3:46:11	3.77
2	EXC38_3_2.5_TESTNAME_161120_2	16/01/2024 16:24:58	3:57:51	3.96
	PSXC38_3_2.5_TESTNAME_161120_2	16/01/2024 16:46:34	4:19:27	4.32
	RPXC38_3_2.5_TESTNAME_161120_2	16/01/2024 16:57:41	4:30:34	4.51
	TaXC38_3_2.5_TESTNAME_161120_2	16/01/2024 17:09:29	4:42:22	4.71
	RPXC382_3_2.5_TESTNAME_161120_2	16/01/2024 18:26:21	5:59:14	5.99
	Z1XC38_3_2.5_TESTNAME_161120_2	16/01/2024 18:38:06	6:10:59	6.18
	RPXC383_3_2.5_TESTNAME_161120_2	16/01/2024 19:59:36	7:32:29	7.54
	PSXC382_3_2.5_TESTNAME_161120_2	16/01/2024 20:11:09	7:44:02	7.73
3	EXC38_3_2.5_TESTNAME_161120_3	16/01/2024 20:22:49	7:55:42	7.93
	PSXC38_3_2.5_TESTNAME_161120_3	16/01/2024 20:44:25	8:17:18	8.29
	RPXC38_3_2.5_TESTNAME_161120_3	16/01/2024 20:55:32	8:28:25	8.47
	TaXC38_3_2.5_TESTNAME_161120_3	16/01/2024 21:07:20	8:40:13	8.67
	RPXC382_3_2.5_TESTNAME_161120_3	16/01/2024 22:24:12	9:57:05	9.95
	Z1XC38_3_2.5_TESTNAME_161120_3	16/01/2024 22:35:57	10:08:50	10.15
	RPXC383_3_2.5_TESTNAME_161120_3	16/01/2024 23:57:27	11:30:20	11.51
	PSXC382_3_2.5_TESTNAME_161120_3	17/01/2024 00:09:00	11:41:53	11.70
4	EXC38_3_2.5_TESTNAME_161120_4	17/01/2024 00:20:40	11:53:33	11.89
	PSXC38_3_2.5_TESTNAME_161120_4	17/01/2024 00:42:16	12:15:09	12.25
	RPXC38_3_2.5_TESTNAME_161120_4	17/01/2024 00:53:23	12:26:16	12.44
	TaXC38_3_2.5_TESTNAME_161120_4	17/01/2024 01:05:11	12:38:04	12.63
	RPXC382_3_2.5_TESTNAME_161120_4	17/01/2024 02:22:03	13:54:56	13.92
	Z1XC38_3_2.5_TESTNAME_161120_4	17/01/2024 02:33:48	14:06:41	14.11
	RPXC383_3_2.5_TESTNAME_161120_4	17/01/2024 03:55:18	15:28:11	15.47
	PSXC382_3_2.5_TESTNAME_161120_4	17/01/2024 04:06:51	15:39:44	15.66
5	EXC38_3_2.5_TESTNAME_161120_5	17/01/2024 04:18:31	15:51:24	15.86
	PSXC38_3_2.5_TESTNAME_161120_5	17/01/2024 04:40:07	16:13:00	16.22
	RPXC38_3_2.5_TESTNAME_161120_5	17/01/2024 04:51:14	16:24:07	16.40
	TaXC38_3_2.5_TESTNAME_161120_5	17/01/2024 05:03:02	16:35:55	16.60
	RPXC382_3_2.5_TESTNAME_161120_5	17/01/2024 06:19:54	17:52:47	17.88
	Z1XC38_3_2.5_TESTNAME_161120_5	17/01/2024 06:31:39	18:04:32	18.08
	RPXC383_3_2.5_TESTNAME_161120_5	17/01/2024 07:53:09	19:26:02	19.43
	PSXC382_3_2.5_TESTNAME_161120_5	17/01/2024 08:04:42	19:37:35	19.63

Appendix C

Under the presented and discussed investigated conditions (~40 h), the working time enabled us to investigate the mechanisms of carbon steel corrosion in SRGW. However, the thickness of the deposits was not sufficient to achieve representative mass loss measurements. Longer experiments were thus conducted.

Corrosion rates, obtained by the gravimetric technique, for CS-XC38 samples immersed for ~5 days in the SRGW in the absence of an inhibitor are presented in Table A6. Two CS-XC38 samples were investigated: the sample named "Disturbed (D)", used for electrochemical measurements, and the sample named "spectator or undisturbed (UD)", used to monitor E_{XC38} in relation to time. CS-XC38/SRGW interaction time corresponds to the time for which the electrodes were immersed in SRGW.

It is obvious that the electrochemical measurements carried out on the disturbed sample caused further corrosion of the steel; this mainly occurred due to disturbing linear polarization at ±250 mV around OCP (Tafel plots). This technique, which is avoided for long-term, in situ corrosion monitoring [37], is nevertheless essential for the investigation of the mechanisms and kinetics of carbon steel corrosion and corrosion inhibition using PS-OCI for screening and optimizing formulas, especially to investigate anodic and cathodic activities.

Only the corrosion of the undisturbed sample makes sense. Please note that these data are not sufficiently representative, as they only cover a few days. However, they can nevertheless be used as an indicator of the corrosion rate of XC38 steel immersed in SRGW.

Table A6. Corrosion rate of CS-XC38 samples immersed in SRGW in the absence of an inhibitor.

CS-XC38 Sample	CS-XC38/SRGW Interaction Time (h)	V_{corr} (mm y^{-1})
UD	118.33	0.425
D	118.33	1.248

References

1. Rojas, J.; Giot, D.; Le Nindre, Y.M.; Criaud, A.; Fouillac, C.; Brach, M.; Menjoz, A.; Martin, J.C.; Lambert, M.; Chiles, J.P.; et al. *Caractérisation et Modélisation du Réservoir Géothermique du Dogger, Bassin Pari-Sien, France, Rapport Final*; BRGM R 30169 IRG SGN 89; BRGM: Orléans, France, 1989; p. 249.
2. Castillo, C.; Ignatiadis, I. Sulfate-Reduction State of the Geothermal Dogger Aquifer, Paris Basin (France) after 35 Years of Exploitation: Analysis and Consequences of Bacterial Proliferation in Casings and Reservoir. In Proceedings of the Thirty-Seventh Workshop on Geothermal Reservoir Engineering, Stanford University, Stanford, CA, USA, 30 January–1 February 2012.
3. Fardeau, M.-L.; Goulhen, F.; Bruschi, M.; Khelifi, N.; Cayol, J.-L.; Ignatiadis, I.; Guyot, F.; Ollivier, B. Archaeoglobus fulgidus and Thermotoga elfii, Thermophilic Isolates from Deep Geothermal Water of the Paris Basin. *Geomicrobiol. J.* **2009**, *26*, 119–130. [CrossRef]
4. Lopez, S.; Hamm, V.; Le Brun, M.; Schaper, L.; Boissier, F.; Cotiche, C.; Giuglaris, E. 40 years of Dogger aquifer management in Ile-de-France, Paris Basin, France. *Geothermics* **2010**, *39*, 339–356. [CrossRef]
5. Peter, F.; Ellis, I. A Geothermal Corrosivity Classification System. *GRC Trans.* **1981**, *5*, 463–472.
6. Ikeda, A.; Mukai, S.; Ueda, M. CO_2 corrosion behavior of carbon and Cr steel. *Sumitomo Search* **1985**, *31*, 91–102.
7. Crolet, J.L. Mécanismes de la corrosion uniforme sous dépôt de corrosion. *Métaux Corros. Ind.* **1998**, *63*, 279–302.
8. Xiao, G.; Tan, S.; Yu, Z.; Dong, B.; Yi, Y.; Tian, G.; Yu, H.; Shi, S. CO_2 corrosion behaviors of 13Cr steel in the high-temperature steam environment. *Petroleum* **2020**, *6*, 106–113. [CrossRef]
9. Soltis, J. Passivity breakdown, pit initiation and propagation of pits in metallic materials—Review. *Corros. Sci.* **2015**, *90*, 5–22. [CrossRef]
10. Evans, U.R. CXL.—The passivity of metals. Part I. The isolation of the protective film. *J. Chem. Soc.* **1927**, 1020–1040. [CrossRef]
11. Frankel, G.S. Pitting Corrosion of Metals: A Review of the Critical Factors. *J. Electrochem. Soc.* **1998**, *145*, 2186. [CrossRef]
12. Pou, T.E.; Murphy, O.J.; Young, V.; Bockris, J.O.M.; Tongson, L.L. Passive Films on Iron: The Mechanism of Breakdown in Chloride Containing Solutions. *J. Electrochem. Soc.* **1984**, *131*, 1243. [CrossRef]
13. Traunbenberg, S.; Foley, R. The influence of chloride and sulphate ions on the corrosion of iron in sulphuric acid. *J. Electrochem. Soc.* **1971**, *118*, 1066–1070. [CrossRef]
14. Galvele, J.R. Transport Processes and the Mechanism of Pitting of Metals. *J. Electrochem. Soc.* **1976**, *123*, 464. [CrossRef]
15. Iofa, Z.A.; Batrakov, V.V.; Ngok, B.C. Influence of anion adsorption on the action of inhibitors on the acid corrosion of iron and cobalt. *Electrochim. Acta* **1964**, *9*, 1645–1653. [CrossRef]
16. Ma, H.; Cheng, X.; Chen, S.; Wang, C.; Zhang, J.; Yang, H. An ac impedance study of the anodic dissolution of iron in sulfuric acid solutions containing hydrogen sulfide. *J. Electroanal. Chem.* **1998**, *451*, 11–17. [CrossRef]

17. Ma, H.; Cheng, X.; Li, G.; Chen, S.; Quan, Z.; Zhao, S.; Niu, L. The influence of hydrogen sulfide on corrosion of iron under different conditions. *Corros. Sci.* **2000**, *42*, 1669–1683. [CrossRef]
18. Pound, B.G.; Wright, B.A.; Sharp, R.M. Electrochemical phases for the iron/sulfur/water under geothermal conditions. *Aust. J. Chem.* **1985**, *38*, 643–657. [CrossRef]
19. Pound, B.G.; Abdurrahman, M.H.; Glucina, P.; Wright, G.A.; Sharp, R.M. The corrosion of carbon steel and stainless steel in simulated geothermal media. *Aust. J. Chem.* **1985**, *38*, 1133–1140. [CrossRef]
20. Hardy, J.A. Utilisation of Cathodic Hydrogen by Sulphate-Reducing Bacteria. *Br. Corros. J.* **1983**, *18*, 190–193. [CrossRef]
21. Amalhay, M.; Akar, A.A.; Ignatiadis, I. Study of scale deposition phenomena in geothermal wells in the Paris Basin. In *The International Symposium, Geothermics 94 in Europe, from Research to Development*; BRGM, Ed.; BRGM: Orléans, France, 1998; pp. 223–232.
22. Lee, W.; Lewandowski, Z.; Nielsen, P.H.; Hamilton, W.A. Role of sulfate-reducing bacteria in corrosion of mild steel: A review. *Biofouling* **1995**, *8*, 165–194. [CrossRef]
23. Rickard, D. The composition of mackinawite. *Am. Min.* **2024**, *109*, 401–407. [CrossRef]
24. Foroulis, Z.A. Closure to "Discussion of 'On the Kinetics of the Breakdown of Passivity of Preanodized Aluminum by Chloride Ions'". *J. Electrochem. Soc.* **1976**, *123*, 841a. [CrossRef]
25. Amalhay, M.; Ignatiadis, I. Comparative Study of the Effectiveness of Various Organic Surfactants in Inhibiting Carbon Steel Corrosion in a Natural Geothermal Environment by Using Rapid Electrochemical Tests. *MSF* **1998**, *289–292*, 169–180. [CrossRef]
26. Blanc, P.; Lassin, A.; Piantone, P.; Azaroual, M.; Jacquemet, N.; Fabbri, A.; Gaucher, E.C. Thermoddem: A geochemical database focused on low temperature water/rock interactions and waste materials. *Appl. Geochem.* **2012**, *27*, 2107–2116. [CrossRef]
27. Parkhurst, D.L.; Appelo, C.A.J. *Description of Input and Examples for PHREEQC Version 3: A Computer Program for Speciation, Batch-Reaction, One-Dimensional Transport, and Inverse Geochemical Calculations*; Techniques and Methods; U.S. Geological Survey: Reston, VA, USA, 2013; p. 519.
28. Marty, B.; Criaud, A.; Fouillac, C. Low enthalpy geothermal fluids from the Paris sedimentary basin—1. Characteristics and origin of gases. *Geothermics* **1988**, *17*, 619–633. [CrossRef]
29. Criaud, A.; Fouillac, C.; Marty, B. Low enthalpy geothermal fluids from the paris basin. 2—Oxidation-reduction state and consequences for the prediction of corrosion and sulfide scaling. *Geothermics* **1989**, *18*, 711–727. [CrossRef]
30. Fouillac, C.; Fouillac, A.M.; Criaud, A. Sulphur and oxygen isotopes of dissolved sulphur species in formation waters from the Dogger geothermal aquifer, Paris Basin, France. *Appl. Geochem.* **1990**, *5*, 415–427. [CrossRef]
31. Thorbjornsson, I.; Kaldal, G.S.; Gunnarsson, B.S.; Ragnarsson, Á. New Approach to Mitigate Casing failures in High-Temperature Geothermal Wells. *GRC Trans.* **2017**, *41*, 585–591.
32. Brioua, S.; Delimi, A.; Ferkous, H.; Boukerche, S.; Allal, H.; Boublia, A.; Djedouani, A.; Berredjem, M.; Kahlouche, A.; Rachedi, K.O.; et al. Enhancing corrosion resistance of XC38 steel using sulfur and nitrogen-containing phenyl thiosemicarbazone: A comprehensive experimental and computational analysis. *J. Taiwan Inst. Chem. Eng.* **2024**, *165*, 105718. [CrossRef]
33. Boulechfar, C.; Ferkous, H.; Djellali, S.; Amin, M.A.; Boufas, S.; Djedouani, A.; Delimi, A.; Amor, Y.B.; Yadav, K.K.; Jeon, B.-H.; et al. DFT/molecular scale, MD simulation and assessment of the eco-friendly anti-corrosion performance of a novel Schiff base on XC38 carbon steel in acidic medium. *J. Mol. Liq.* **2021**, *344*, 117874. [CrossRef]
34. Mouats, N.; Djellali, S.; Ferkous, H.; Sedik, A.; Delimi, A.; Boublia, A.; Rachedi, K.O.; Berredjem, M.; Çukurovali, A.; Alam, M.; et al. Comprehensive Investigation of the Adsorption, Corrosion Inhibitory Properties, and Quantum Calculations for 2-(2,4,5-Trimethoxybenzylidene) Hydrazine Carbothioamide in Mitigating Corrosion of XC38 Carbon Steel under HCl Environment. *ACS Omega* **2024**, *9*, 27945–27962. [CrossRef]
35. Wamba-Tchio, O.R.; Pengou, M.; Teillout, A.-L.; Baumier, C.; Mbomekallé, I.M.; De Oliveira, P.; Nanseu-Njiki, C.P.; Ngameni, E. Electrochemical study and experimental simulation of the synergistic effect of a formulation based on Ficus pumila Linn. Leaves extract and zinc sulfate on the XC38 steel corrosion inhibition in NaCl solution. *J. Electroanal. Chem.* **2022**, *919*, 116553. [CrossRef]
36. Ichchou, I.; Larabi, L.; Rouabhi, H.; Harek, Y.; Fellah, A. Electrochemical evaluation and DFT calculations of aromatic sulfonohydrazides as corrosion inhibitors for XC38 carbon steel in acidic media. *J. Mol. Struct.* **2019**, *1198*, 126898. [CrossRef]
37. Moyeme, Y.C.S.; Betelu, S.; Bertrand, J.; Serrano, K.G.; Ignatiadis, I. Corrosion Current Density of API 5L X65 Carbon Steel in Contact with Natural Callovian-Oxfordian Clay Pore Water, Assessed by Various Electrochemical Methods over 180 Days. *Metals* **2023**, *13*, 966. [CrossRef]
38. Orazem, M.E.; Tribollet, B. *Electrochemical Impedance Spectroscopy*; The Electrochemical Society Series; John Wiley & Sons, Inc.: Pennington, NJ, USA, 2008; p. 526.
39. Barsoukov, E.; Macdonald, J.R. *Impedance Spectroscopy: Theory, Experiment, and Applications*; The Electrochemical Society Series; John Wiley & Sons, Inc.: Hoboken, NJ, USA, 2018; p. 606.
40. Stern, M.; Geary, A.L. Electrochemical Polarization: I. A Theoretical Analysis of the Shape of Polarization Curves. *J. Electrochem. Soc.* **1957**, *104*, 56. [CrossRef]
41. Bard, A.J.; Faulkner, L.R. *Electrochemical Methods: Fundamentals and Applications*; Wiley: New York, NY, USA, 1980.
42. *ASTM G1-90*; Standard Practice for Preparing, Cleaning, and Evaluating Corrosion Test Specimens. ASTM International: West Conshohocken, PA, USA, 2017.
43. Panchenko, Y.M.; Marshakov, A.I.; Igonin, T.N.; Kovtanyuk, V.V.; Nikolaeva, L.A. Long-term forecast of corrosion mass losses of technically important metals in various world regions using a power function. *Corros. Sci.* **2014**, *88*, 306–316. [CrossRef]

44. Skoog, D.; West, D.M.; Holler, F.J.; Fort, W. *Gravimetric Analysis. Fundamentals of Analytical Chemistry*, 7th ed.; Saunders College Publishing: Fort Worth, TX, USA, 1996; p. 870.
45. Daoudi, J.; Betelu, S.; Tzedakis, T.; Bertrand, J.; Ignatiadis, I. A Multi-Parametric Device with Innovative Solid Electrodes for Long-Term Monitoring of pH, Redox-Potential and Conductivity in a Nuclear Waste Repository. *Sensors* **2017**, *17*, 1372. [CrossRef]
46. Shoesmith, D.W.; Taylor, P.; Bailey, M.G.; Owen, D.G. The Formation of Ferrous Monosulfide Polymorphs during the Corrosion of Iron by Aqueous Hydrogen Sulfide at 21 °C. *J. Electrochem. Soc.* **1980**, *127*, 1007. [CrossRef]
47. Chivot, J. *Thermodynamique des Produits de Corrosion: Fonctions Thermodynamiques, Diagrammes de Solubilité, Diagrammes E-ph des Systèmes Fe-H_2O, Fe-CO_2-H_2O, Fe-S-H_2O, Cr-H_2O et Ni-H_2O en Fonction de la Temperature*; Andra: Chatenay-Malabry, France, 2004; 142p, ISBN 2-9510108-6.
48. Brigham, R.J.; Tozer, E.W. Temperature as a Pitting Criterion. *Corrosion* **2013**, *29*, 33–36. [CrossRef]
49. Ovarfort, R. Critical pitting temperature measurements of stainless steels with an improved electrochemical method. *Corros. Sci.* **1989**, *29*, 987–993. [CrossRef]